

# **Ruthenium Metal Complexes in Anticancer Activity**

**M.Sc. Thesis**

By

**SRIJITA PAL**



**DEPARTMENT OF CHEMISTRY  
INDIAN INSTITUTE OF TECHNOLOGY  
INDORE**

**May 2023**



# **Ruthenium Metal Complexes in Anticancer Activity**

**A THESIS**

*Submitted in partial fulfillment of the  
requirements for the award of the degree  
of*  
**Master of Science**

*by*  
**SRIJITA PAL**



**DEPARTMENT OF CHEMISTRY  
INDIAN INSTITUTE OF TECHNOLOGY  
INDORE**

**MAY 2023**





# INDIAN INSTITUTE OF TECHNOLOGY INDORE

## CANDIDATE'S DECLARATION

I hereby certify that the work which is being presented in the thesis entitled “**Ruthenium Metal Complexes in Anticancer Activity**” in the partial fulfillment of the requirements for the award of the degree of **MASTER OF SCIENCE** and submitted in the **DEPARTMENT OF CHEMISTRY, INDIAN INSTITUTE OF TECHNOLOGY INDORE**, is an authentic record of my own work carried out during the time period from July 2022 to May 2023 under the supervision of **Dr. Suman Mukhopadhyay**, Professor, IIT Indore.

The matter presented in this thesis has not been submitted by me for the award of any other degree of this or any other institute.

*Srijita Pal*  
**SRIJITA PAL**

-----  
This is to certify that the above statement made by the candidate is correct to the best of my knowledge.

*Suman Mukhopadhyay*  
**Prof. Suman Mukhopadhyay**

-----  
SRIJITA PAL has successfully given her M.Sc. Oral Examination held on **16 May 2023**.

*Suman Mukhopadhyay*  
Signature of Supervisor of MSc thesis  
**Prof. Suman Mukhopadhyay**  
Date: *19/05/2023*

*Umesh A. Kshirsagar*  
Convener, DPGC  
**Dr. Umesh A. Kshirsagar**  
Date: *23/05/2023*

*Sampak Samanta*  
Signature of PSpC Member 1  
**Prof. Sampak Samanta**  
Date: *19/05/2023*

*Umesh A. Kshirsagar*  
Signature of PSpC Member 2  
**Dr. Umesh A. Kshirsagar**  
Date: *23/05/2023*



# ACKNOWLEDGEMENTS

First and foremost, I would like to express my heartfelt gratitude to my thesis supervisor Prof. Suman Mukhopadhyay for his constant guidance, support, cooperation and encouragement. I am fortunate enough to have the opportunity of working under his kind supervision and learning from him.

I would also like to extend my gratitude to my PSPC members Prof. Sampak Samanta and Dr. Umesh A. Kshirsagar, for their sincere recommendation and motivation. I thank Dr. Tushar Kanti Mukherjee, Head of Department, Chemistry and DPGC Convenor Dr. Umesh A. Kshirsagar for their suggestions and assistance.

I also want to express my gratitude to Prof. Suhas Joshi, Director, IIT Indore for providing the resources and a stimulating research environment.

I would also take this opportunity to thank SIC, IIT Indore and Chemistry Office for their assistance and technical support, without which it would not have been possible to work on this project.

I also thank my mentor Ms. Pragti for guiding me and assisting me in every step which helped me in making progress in this project. I would also like to thank my lab mates for their constant encouragement.

I also acknowledge with a deep sense of reverence towards my parents and my family members, who have always supported me morally and encouraged me.

It is the kindness of these acknowledged persons that I have been able to make progress in this project successfully. Without their guidance I would not have made any headway in this research project.

**SRIJITA PAL**

Department of Chemistry, IIT Indore



***Dedicated to...***

*Maa, Bapi and Dadabhai for always  
supporting me and motivating me*



## ABSTRACT

The discovery of first anticancer drug cisplatin was a path breaker in the world of medicinal chemistry, but due to undesirable side effects and acquired resistance over years, scientists are searching for alternative strategies involving novel metal-based compounds having improved pharmacological properties. Ruthenium complexes have emerged as prospective candidates to combat the side effects and improve the selectivity of anticancer agents. In this work a benzimidazole based chelating ligand **HL** (**4-(1*H*-Naphth[2,3-*d*]imidazol-2-yl)-1,3-benzenediol**) with O and N as donor centres was synthesized, and was used for complexation with ruthenium to obtain three Ru(II) arene complexes represented by  $[\text{Ru}(\eta^6\text{-}p\text{-cym})(\text{L})(\text{X})]$  or  $[\text{Ru}(\eta^6\text{-}p\text{-cym})(\text{L})(\text{X})]^+$  (where *p*-cym = *p*-cymene, X = (i) Cl, (ii) PPh<sub>3</sub> = triphenyl phosphine, (iii) PTA = 1,3,5-triaza-7-phosphaadamantane). The synthesized complexes were characterized using mass spectrometry, NMR spectroscopy, FTIR, UV-Vis and fluorescence spectroscopy. Using absorption spectroscopy the stability of the complexes in biological medium was analysed and partition coefficient in *n*-octanol and water was calculated to study the lipophilicity of the complexes. The complexes showed significant binding with biomolecules like albumin proteins and nucleic acids. All the complexes were found to be cytotoxic with complex  $[\text{Ru}(\eta^6\text{-}p\text{-cym})(\text{L})\text{PPh}_3]\text{PF}_6$  exhibiting the highest anticancer activity. The mechanism of anticancer activity was attributed to the ability of the complexes to induce apoptosis and generate reactive oxygen species (ROS). The complexes also exhibited antimetastatic property. Further complex  $[\text{Ru}(\eta^6\text{-}p\text{-cym})(\text{L})\text{PPh}_3]\text{PF}_6$  was loaded on amine functionalized mesoporous silica nanoparticles which lead to an increase in its cytotoxic activity. The drug loaded nanoparticles were characterized using several characterization techniques like IR, UV-Vis spectroscopy, PXRD, FE-SEM, TGA and BET.



## TABLE OF CONTENTS

<b>LIST OF FIGURES</b>	xiii
<b>LIST OF SCHEMES</b>	xvii
<b>LIST OF TABLES</b>	xviii
<b>NOMENCLATURE</b>	ix
<b>ACRONYMS</b>	xx
<b>Chapter 1: Introduction</b>	<b>1-6</b>
1.1 1.1 Metal Based Medicines	1-2
1.2 Ruthenium Complexes as Anticancer Agents	2-3
1.3 RAPTA Complexes	3-4
1.4 Choice of Ligands	4-5
1.5 MSNs- Delivery Vehicles for Anticancer Drugs	5-6
1.6 Organization of Thesis	6
<b>Chapter 2: Past Work</b>	<b>7-12</b>
2.1 Review of Past Work and Project Motivation	7-12
<b>Chapter 3: Experimental Section</b>	<b>13-22</b>
3.1 Reagents and Chemicals	13
3.2 Methods and Instrumentation	13
3.3 Synthesis of Ruthenium Dimer, Ligand and Metal Complexes	14-15
3.4 Synthesis of MSNs, A-MSNs and C2@A-MSNs	16
3.5 Stability Study	17
3.6 Lipophilicity Study	17
3.7 Protein Binding Study	18
3.8 Nucleic Acid Binding Study	19
3.9 Drug Release Study	19-20
3.10 Cell Viability Assay	20-21
3.11 Apoptosis Study using Dual Staining Method	21
3.12 ROS Generation- DCFH-DA Assay	21-22
3.13 Metastasis Inhibition	22

<b>Chapter 4: Results and Discussions</b>	<b>23-56</b>
4.1 Structure and Synthesis	23
4.2 Reaction Schemes	23-25
4.3 Characterization	25-39
4.4 Stability Study	39-40
4.5 Lipophilicity Study	40-41
4.6 Protein Binding Study	41-44
4.7 Nucleic Acid Binding Study	45-48
4.8 Drug Loading and pH Stimulated Release	49-50
4.9 Cell Viability Assay	50-52
4.10 Apoptosis Study using Dual Staining Method	52-53
4.11 ROS Generation- DCFH-DA Staining	54
4.12 Metastasis Inhibition	55-56
<b>Chapter 5: Conclusion and Future Scope</b>	<b>57-58</b>
<b>References</b>	<b>59-63</b>

## LIST OF FIGURES

<b>Figure</b>	<b>Description</b>	<b>Page No.</b>
<b>Figure 1.1</b>	Structure of (A) KP1019 and (B) NAMI-A	3
<b>Figure 1.2</b>	Structure of RAPTA-C and RAPTA-T	4
<b>Figure 1.3</b>	Structure activity relationship of different ligands	5
<b>Figure 2.1</b>	Synthesis of Ru(II) arene complexes using a pyrene based fluorescent ligand	7
<b>Figure 2.2</b>	Synthesis of RAPTA complexes using curcumin as the leaving group	9
<b>Figure 2.3</b>	Synthesis of Ru(II) complexes with varying co-ligands and their effect on cytotoxicity	9
<b>Figure 2.4</b>	Chitosan-Biotin conjugated MSNs for aggregated drug delivery	10
<b>Figure 2.5</b>	Improved cytotoxicity upon loading Ru(II) complex on A-MSNs	11
<b>Figure 4.1</b>	Mass spectrum of <b>HL</b>	26
<b>Figure 4.2</b>	Mass spectrum of <b>C1</b>	26
<b>Figure 4.3</b>	Mass spectrum of <b>C2</b>	26
<b>Figure 4.4</b>	Mass spectrum of <b>C3</b>	27
<b>Figure 4.5</b>	<sup>1</sup> H NMR spectrum of <b>HL</b>	28
<b>Figure 4.6</b>	<sup>13</sup> C NMR spectrum of <b>HL</b>	28
<b>Figure 4.7</b>	<sup>1</sup> H NMR spectrum of <b>C1</b>	29
<b>Figure 4.8</b>	<sup>13</sup> C NMR spectrum of <b>C1</b>	29
<b>Figure 4.9</b>	<sup>1</sup> H NMR spectrum of <b>C2</b>	30
<b>Figure 4.10</b>	<sup>13</sup> C NMR spectrum of <b>C2</b>	31
<b>Figure 4.11</b>	<sup>31</sup> P NMR spectrum of <b>C2</b>	31
<b>Figure 4.12</b>	<sup>1</sup> H NMR spectrum of <b>C3</b>	32
<b>Figure 4.13</b>	<sup>13</sup> C NMR spectrum of <b>C3</b>	33
<b>Figure 4.14</b>	<sup>31</sup> P NMR spectrum of <b>C3</b>	33
<b>Figure 4.15</b>	FTIR Spectra of (a) ligand <b>HL</b> (b) complex	35

	<b>C1, (c) complex C2 (d) complex C3</b>	
<b>Figure 4.16</b>	FTIR Spectra depicting (a) amine functionalization of <b>MSNs</b> (b) Loading of <b>C2</b> on <b>A-MSNs</b>	35
<b>Figure 4.17</b>	UV- Vis absorption spectra of (a) ligand <b>HL</b> and complexes <b>C1, C2, C3</b> (b) <b>MSNs, A-MSNs</b> and <b>C2@A-MSNs</b>	36
<b>Figure 4.18</b>	Fluorescence spectra of ligand <b>HL</b> and complexes <b>C1, C2, C3</b>	37
<b>Figure 4.19</b>	Powder XRD patterns for (a) <b>MSN</b> (b) <b>A-MSNs</b>	37
<b>Figure 4.20</b>	(i) TGA curve of (a) <b>MSNs</b> , (b) <b>A-MSNs</b> (c) <b>C2@A-MSNs</b> (ii) N <sub>2</sub> adsorption isotherms of (a) <b>MSNs</b> , (b) <b>A-MSNs</b> (c) <b>C2@ A-MSNs</b>	38
<b>Figure 4.21</b>	SEM images of (a) <b>MSN</b> and (b) <b>A-MSN</b> (c) <b>C2@A-MSNs</b>	39
<b>Figure 4.22</b>	Stability study of (a) complex <b>C1</b> , (b) complex <b>C2</b> , (c) complex <b>C3</b> in DMSO/PBS buffer solution (d) complex <b>C2</b> in PBS buffer (pH- 5.4)	40
<b>Figure 4.23</b>	Fluorometric titration spectra of BSA (10 μM) with (a) ligand <b>HL</b> , (b) complex <b>C1</b> , (c) complex <b>C2</b> , and (d) complex <b>C3</b> at 298 K	42
<b>Figure 4.24</b>	Fluorometric titration spectra of HSA (10 μM) with (a) ligand <b>HL</b> , (b) complex <b>C1</b> , (c) complex <b>C2</b> , and (d) complex <b>C3</b> at 298 K	42
<b>Figure 4.25</b>	Stern Volmer plots for the titration of BSA with (a) ligand <b>HL</b> , (b) complex <b>C1</b> , (c) complex <b>C2</b> , (d) complex <b>C3</b>	43
<b>Figure 4.26</b>	Stern Volmer plots for the titration of HSA with (a) ligand <b>HL</b> , (b) complex <b>C1</b> , (c) complex <b>C2</b> , (d) complex <b>C3</b>	44
<b>Figure 4.27</b>	Titration of (a) ligand <b>HL</b> , (b) complex <b>C1</b> ,	45

	(c) complex <b>C2</b> , and (d) complex <b>C3</b> with increasing amount of CT-DNA at 298 K using UV-Vis spectroscopy	
<b>Figure 4.28</b>	Fluorometric titration spectra of CT-DNA (10 $\mu$ M) with (a) ligand <b>HL</b> , (b) complex <b>C1</b> , (c) complex <b>C2</b> , and (d) complex <b>C3</b> at 298 K	46
<b>Figure 4.29</b>	Fluorometric titration spectra of RNA (10 $\mu$ M) with (a) ligand <b>HL</b> , (b) complex <b>C1</b> , (c) complex <b>C2</b> and (d) complex <b>C3</b> at 298 K	47
<b>Figure 4.30</b>	Stern Volmer plots for binding of DNA with (a) ligand <b>HL</b> , (b) complex <b>C1</b> , (c) complex <b>C2</b> , (d) complex <b>C3</b>	47
<b>Figure 4.31</b>	Stern Volmer plots for binding of RNA with (a) ligand <b>HL</b> , (b) complex <b>C1</b> , (c) complex <b>C2</b> , (d) complex <b>C3</b>	48
<b>Figure 4.32</b>	Drug release profile for <b>C2@A-MSNs</b> in acidic and neutral pH	49
<b>Figure 4.33</b>	Probable mechanism of drug release from <b>A-MSNs</b>	50
<b>Figure 4.34</b>	Mass spectrum of released complex from <b>A-MSNs</b>	50
<b>Figure 4.35</b>	Cell viability curves for ligand <b>HL</b> , complex <b>C1</b> , <b>C2</b> , <b>C3</b> and <b>C2@A-MSNs</b> on (a) HeLa cell lines (b) DU145 cell lines and (c) HEK 293 (normal cell lines)	51
<b>Figure 4.36</b>	Histogram representing the $IC_{50}$ values in ( $\mu$ M) of the ligand, three complexes and <b>C2@A-MSNs</b> for cancer cells lines (a) HeLa, (b) DU145 and (c) normal cells HEK 293	52
<b>Figure 4.37</b>	Confocal images of Hela cells stained with AO and EtBr after treatment with the complexes	53
<b>Figure 4.38</b>	ROS generation using DCFH-DA Assay and	54

fluorescence intensity graph for ROS  
generation

- Figure 4.39** Wound healing motility assay of HeLa 55  
untreated and treated cell with the free  
complexes as well as **C2@A-MSNs**. Images  
were taken at 0 and 24 h.
- Figure 4.40** Histogram representing percentage wound 56  
closure ratio after 24 hours

## LIST OF SCHEMES

<b>Scheme</b>	<b>Description</b>	<b>Page No.</b>
<b>Scheme 4.1</b>	Reaction scheme for the synthesis of dimer	23
<b>Scheme 4.2</b>	Reaction scheme for the synthesis of ligand <b>HL</b>	24
<b>Scheme 4.3</b>	Reaction scheme for the synthesis of complexes <b>C1, C2, C3</b>	24
<b>Scheme 4.4</b>	Reaction scheme for the synthesis of <b>MSNs</b>	24
<b>Scheme 4.5</b>	Reaction scheme for amine functionalization of <b>MSNs</b>	25
<b>Scheme 4.6</b>	Reaction scheme for loading of <b>C2</b> on <b>A- MSNs</b>	25

## LIST OF TABLES

<b>Table</b>	<b>Description</b>	<b>Page No.</b>
<b>Table 4.1</b>	Excitation and emission wavelengths of ligand <b>HL</b> and complexes <b>C1, C2, C3</b>	37
<b>Table 4.2</b>	Characteristic parameters of <b>MSN</b> and <b>A-MSNs</b> observed from N <sub>2</sub> adsorption-desorption experiment	39
<b>Table 4.3</b>	Partition coefficient value for the complexes <b>C1, C2</b> and <b>C3</b>	41
<b>Table 4.4</b>	Various parameters to analyze the binding between proteins and the compounds from <b>SV</b> and Scatchard plots	44
<b>Table 4.5</b>	Various parameters to analyze the binding between nuclei acids and the compounds from <b>SV</b> and Scatchard plots	48
<b>Table 4.6</b>	IC <sub>50</sub> values in (μM) of the ligand, three complexes and <b>C2@A-MSNs</b> for cancer cells HeLa and DU145 and normal cells HEK 293	52

## NOMENCLATURE

$\text{\AA}$	Angstrom
$K_q$	Bimolecular Quenching Constant
$K_a$	Binding Constant
cm	Centimetre
$\delta$	Chemical Shift (NMR)
$^{\circ}\text{C}$	Degree Centigrade
$\tau$	Fluorescence Lifetime
$\nu$	Frequency
gm	Gram
K	Kelvin
L	Litre
$\mu\text{L}$	Micro Litre
$\mu\text{M}$	Micro Molar
mL	Milli Litre
mM	Milli Molar
mmol	Milli Mole
mol	Mole
n	No. of binding sites
nm	Nanometre
%	Percentage
$K_{sv}$	Stern Volmer Constant
$\lambda$	Wavelength

## ACRONYMS

<b>A-MSNs</b>	Amine functionalized MSNs
<b>AO</b>	Acridine Orange
<b>APTES</b>	(3-Aminopropyl)triethoxysilane
<b>BET</b>	Brunauer-Emmett-Teller
<b>BSA</b>	Bovine Serum Albumin
<b>CO<sub>2</sub></b>	Carbon Dioxide
<b>CTAB</b>	Cetyltrimethylammonium bromide
<b>CT-DNA</b>	Calf Thymus DNA
<b>DMEM</b>	Dulbecco's modified Eagle medium
<b>DMF</b>	Dimethylformamide
<b>DMSO</b>	Dimethylsulphoxide
<b>DNA</b>	Deoxyribonucleic acid
<b>ESI-MS</b>	Electron Spray Ionisation- Mass Spectrometry
<b>EtBr</b>	Ethidium Bromide
<b>FBS</b>	Fetal Bovine Serum
<b>FE-SEM</b>	Field Emission Scanning Electron Microscope
<b>FT-IR</b>	Fourier Transform- Infrared
<b>HSA</b>	Human Serum Albumin
<b>IC<sub>50</sub></b>	Half maximal inhibitory concentration
<b>MSNs</b>	Mesoporous silica nanoparticles
<b>NMR</b>	Nuclear Magnetic Resonance
<b>ROS</b>	Reactive Oxygen Species
<b>Ru</b>	Ruthenium
<b>PBS</b>	Phosphate buffered saline
<b>Ppm</b>	Parts per million
<b>PXRD</b>	Powder X-Ray Diffraction
<b>TGA</b>	Thermogravimetric analysis
<b>TEOS</b>	Tetraethyl orthosilicate
<b>Tris-HCl</b>	Tris-hydrochloric acid
<b>RNA</b>	Ribonucleic acid
<b>UV</b>	Ultraviolet

# *Chapter 1*

## **INTRODUCTION**

Cancer is a disease which occurs when cells start dividing in an uncontrollable manner and spread to different parts of the body. There can be several reasons for this genetic change like exposure to certain chemicals, viruses or UV radiation. It can also be caused due to inheritance of genes from the previous generation. In 2020 nearly 10 million deaths were reported due to cancer making it a leading cause of death [1].

### **1.1 Metal Based Medicines**

Metal ions play a crucial role in living systems. They are present in various enzymes and cofactors, and are used in various biological processes like electron transfer reactions. In addition to this, they are also used in designing drugs (the well-known anticancer drug cisplatin), diagnostic agents (Gd and Mn are used for MRI contrasting agents) and used as photosensitizer in photodynamic therapy (PDT) [2]. The discovery of cisplatin in 1960s by Barnett Rosenberg was a path breaker in the field of medicinal chemistry. Since, then researchers have tried to incorporate metal ions as a scaffold to orientate organic ligands and optimize their binding properties with biomolecules. The ability of metal complexes to exhibit different geometry, varying coordination number and variable oxidation states has been exploited to develop new drugs. Since, the discovery of cisplatin, several platinum based drugs have been discovered as anticancer agents but only three of them namely cisplatin (1), carboplatin (2), and oxaliplatin (3) have been clinically approved worldwide. The mode of action of cisplatin involves substitution of the labile chloride ligand by the electron rich N7 of guanine nucleobase of DNA, leading to cell apoptosis. Cisplatin, despite being affective against lung, head, ovarian, neck and oesophageal cancers have several disadvantages like toxicity arising due to the lack of specificity towards cancerous cells over normal cells. Another issue is, with time

cancer cells acquire resistance towards cisplatin. The problem of selectivity and toxicity can be resolved using nanotechnology but the issue of chemoresistance can only be solved by switching to alternating metal ions that may have a different mechanistic pathway [3-7].

## **1.2 Ruthenium Complexes as Anticancer Agents**

The ability of ruthenium to exhibit variable stable oxidation states, preference for hexa-coordinated octahedral geometry and lower toxicity than platinum based drugs have gained significance attention in the past few years. The hexa-coordinated octahedral geometry helps in modulating the steric and electronic properties of the complex by introducing desired ligands [8]. For ruthenium(II) complexes the ligand exchange rate was observed similar to platinum(II) complex which matches with the cell division process making it a suitable alternative for platinum based drugs [9]. In addition, since ruthenium belongs to the same group as iron it can be easily transported by transferrin, which is overexpressed in cancerous cells, thereby facilitating cellular uptake selectively in tumour cells. The advancement of few ruthenium(III) drugs namely NAMI-A (imidazolium trans-[tetrachloro (dimethylsulfoxide) (1H-imidazole) ruthenium(III)]), KP1019 (indazolium trans-[tetrachlorobis(1H-indazole)ruthenium(III)]), and NKP-1339, the sodium salt of KP1019 has made researchers work extensively on ruthenium based complexes. These ruthenium(III) complexes get activated inside the cancer cells where the hypoxic environment, acidic pH and high levels of glutathione reduces it to ruthenium(II) [4-7].

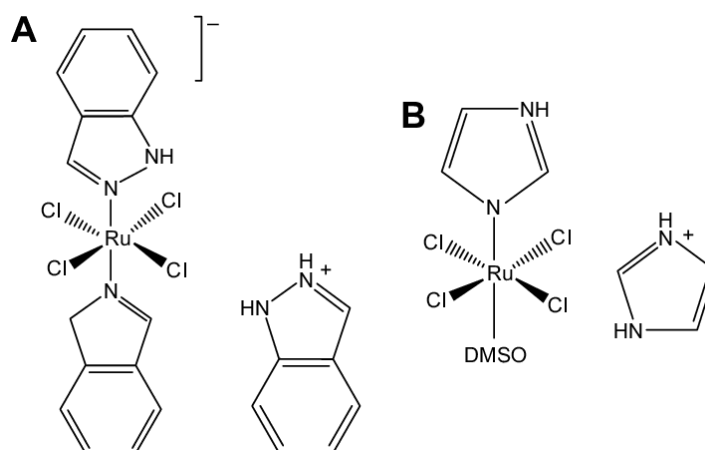


**Figure 1.1:** Structure of (A) KP1019 and (B) NAMI-A

Ruthenium being electron deficient interacts with the electron rich nucleobases of DNA causing unwinding of its helical structure and disrupting DNA based processes which are essential in the rapid cell division process in cancer cells [3]. In addition to targeting genetic material like DNA, organometallic ruthenium complex having suitable moieties can also act as multi-targeted drugs by targeting certain enzymes, peptides and intracellular proteins that are overexpressed in tumour cells [4]. The studies with NAMI-A and KP1019 have been currently paused due to the poor solubility of KP1019 and nephrotoxicity arising from NAMI-A. However two other ruthenium complexes,  $[\text{Ru}(\eta^6\text{-}p\text{-cymene})\text{Cl}_2(1,3,5\text{-triazol-7-phosphadmantane})]$  or RAPTA-C, and KP1339 (sodium salt of KP1019) are currently undergoing clinical trials [10-12].

### 1.3 RAPTA Complexes

Other than ruthenium(III) complexes, several ruthenium(II) arene complexes having piano stool geometry have shown promising anticancer activity. Inspired by the working of cisplatin which involves the presence of a labile chloride ligand, several ruthenium(II) arene complexes have been synthesized with the general formula  $[(\eta^6\text{-arene})\text{Ru}(\text{X})(\text{Y})(\text{Z})]$ , where X and Y represents two monodentate ligands or a single bidentate ligand and Z represents the labile ligand

which can easily undergo dissociation facilitating the coordination of ruthenium to biomolecules. The arene ring plays a role in increasing the reactivity of the complexes. It lowers the  $pK_a$  value facilitating the water exchange rate [13-14].

RAPTA complexes consists of a arene moiety which imparts hydrophobic character to the complex thereby facilitating its transportation through the hydrophobic lipid bilayer of the cellular membrane, and PTA (1,3,5-triaza-7-phosphatricyclo-[3.3.1.1] decane), because of its water soluble nature results in the overall amphiphilic nature of the ruthenium(II) complex [15]. RAPTA complexes are known to have comparable antimetastatic activity with NAMI-A. RAPTA-C and RAPTA-T which contains *p*-cymene and toluene group respectively though are not very cytotoxic but can successfully stop metastasis in the lungs of mice that were infected with mammary carcinoma. RAPTA-C complexes are also effective in case of primary tumours for colorectal and ovarian cancers [3].

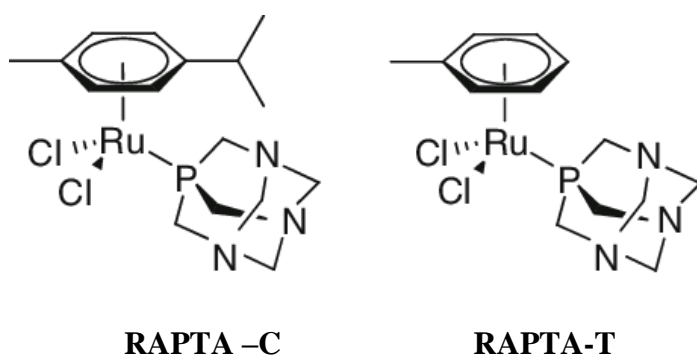


*Figure 1.2: Structure of RAPTA-C and RAPTA-T*

## **1.4 Choice of Ligands**

Along with the central metal ion, the ligands coordinated to it are also responsible for the efficiency of the complex as a drug. The dicarboxylate chelating ligand in carboplatin confers greater stability to the complex resulting in lower side effects than cisplatin [7]. Thus, by proper choice of ligands the biological properties of ruthenium complexes can be modulated [16]. The imine group present in Schiff bases can form intermolecular hydrogen bonds with intracellular active

components resulting in its wide range of pharmacological applications. Incorporating ligands having extensive  $\pi$ -conjugation like phenanthroline, anthracene, naphthalene and pyrene derivatives render fluorescent nature to the complexes making them suitable for monitoring the probable mechanism of anticancer activity [17]. Nitrogen containing heterocycles like benzimidazoles are similar in structure with purine base of DNA leading to easy recognition by biological targets and wide biological activity [18]. Ancillary bidentate ligands can also interact with biomolecules through hydrogen bonding or intercalation thereby controlling the reactivity [19].

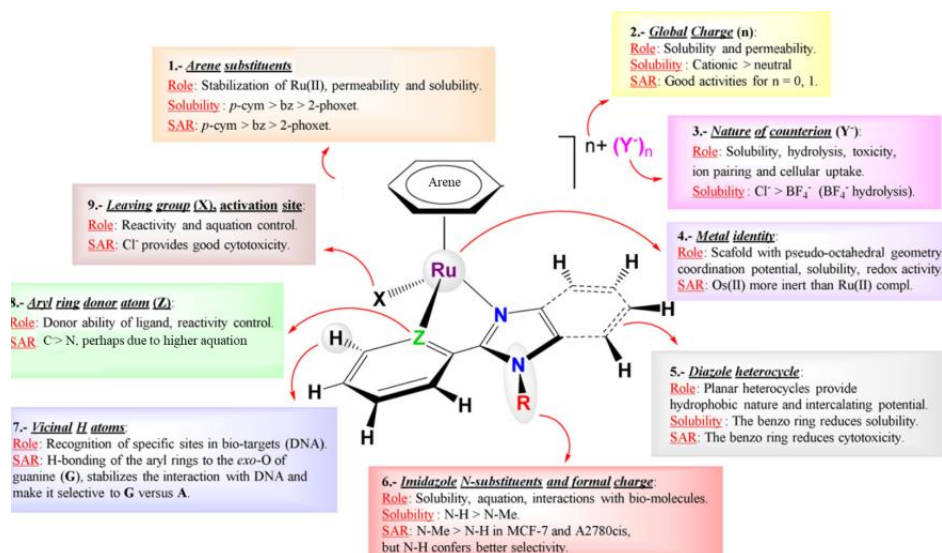


**Figure 1.3:** Structure activity relationship of different ligand. Reproduced with permission from ref. 19. Copyright 2014 American Chemical Society

## 1.5 MSNs – Delivery Vehicles for Anticancer Drugs

To improve the therapeutic potential of drugs several nanocarriers have been developed to selectively deliver the drug to the desired target. Among several drug delivery systems mesoporous silica nanoparticles (MSNs) because of certain advantages like large surface area enabling efficient loading of drug, tunable pore size and morphology, excellent biocompatibility, stability, sustained drug release profile and ability to transport hydrophobic drugs have emerged as an efficient method [20]. Particularly, amine functionalized MSNs (A-MSNs) are known in

literature for improved cellular uptake of cationic ruthenium complexes arising due to strong interaction between positively charged surface of A-MSNs and negatively charged phospholipids of the cell membrane. The silica nanoparticles are also known to selectively deliver the drug to the cancer cells as they have a better drug release profile in acidic environment which differentiates cancer cells from normal cells [21].

## **1.5 Organization of the Thesis**

**Chapter 1:** This chapter briefly describes about cancer, the use of metals in medicine and cisplatin, ruthenium compounds as a prospective candidate for anticancer activity, the efficiency of ruthenium arene compounds in particular, the importance of choice of ligands and the use of MSNs for targeted drug delivery.

**Chapter 2:** This chapter contains the review of some of the past work done in this topic and the motivation behind this work.

**Chapter 3:** This chapter includes the materials, instrumentation, procedure for the synthesis of ligands, complexes, MSNs, functionalization of MSNs and loading of drug on A-MSNs, experimental procedure for stability study, lipophilicity study, protein binding interactions, DNA binding interactions, cell viability assay, apoptosis study using dual staining assay, ROS generation using DCFH-DA assay and antimetastatic property.

**Chapter 4:** This chapter discusses all the results and the findings of the project.

**Chapter 5:** This chapter concludes and summarizes the work done and discusses the future scope of the project.

## Chapter 2

### PASTWORK

#### 2.1 Review of Past Work and Project Motivation

The ruthenium(III) complexes, NAMI-A, KP1019, NKP-1339, the sodium salt of KP1019 that have successfully entered clinical trials act as pro-drugs and get activated inside the hypoxic environment of tumour cells where it is reduced to ruthenium(II) [4]. Thus, several ruthenium(II) arene complexes having piano stool geometry have been synthesized over the past few years.

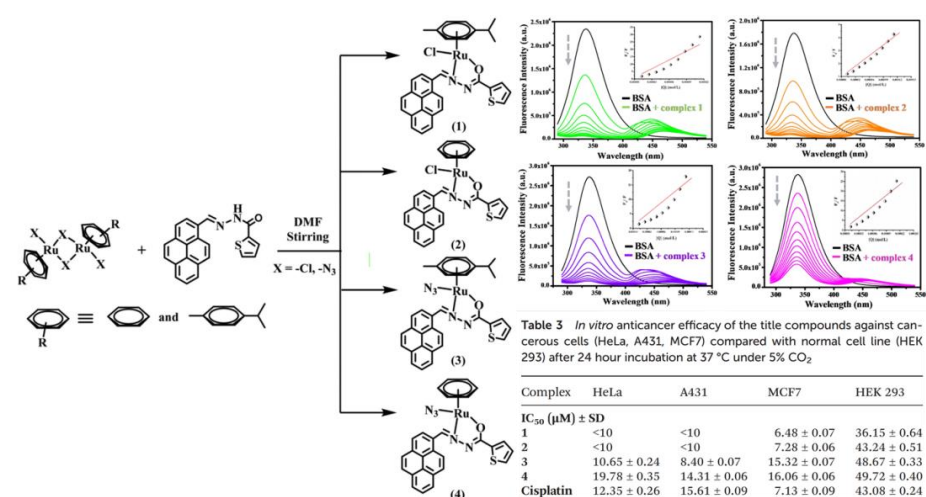


**Figure 2.1:** Synthesis of Ru(II) arene complexes using a pyrene based fluorescent ligand. Reproduced from ref. 17 with permission from The Royal Society of Chemistry

In a recent report by Pragti *et al.*, four pyrene based ruthenium(II) complexes have been synthesized and further investigated to see whether they are effective against cancer. The pyrene containing schiff base chelating ligand with N, O as donor atoms imparted fluorescent nature to the complex which was exploited to reveal the mechanism of action. Spectroscopic studies indicated significant interaction between the complexes and biomolecules like proteins and DNA. MTT colorimetric assay suggested that all the complexes exhibited good cytotoxicity against MCF7, HeLa and A431 cell lines. Complex 1 and 2 was found to be more effective because of the presence of the labile

chloride ligand which facilitated the ligand water exchange reaction and the hydrophobic *p*-cymene group which lead to better interaction with biomolecules. The complexes can also generate ROS by catalysing the reaction where NADH is oxidized to NAD<sup>+</sup> [17].

The choice of ligand plays an important role in designing ruthenium complexes having potential anticancer activity. Heterocyclic ligands containing nitrogen have found significant applications in pharmaceuticals due to its similarity in structure with natural molecules. In particular benzimidazole containing compounds are well known for exhibiting a vast array of biological applications including antimicrobial, fungal, analgesics, antidiabetic and anticancer properties. Due to their electron rich environment and easy coordination with metal centres several benzimidazole based transition metal complexes are reported in medicinal inorganic chemistry [18].

In a previously reported paper by H.A. Sahyon *et al.*, ruthenium complexes of 2-aminophenyl benzimidazole were synthesized and their anticancer activity was investigated. MTT assay was performed and it was observed that the complexes showed good cytotoxicity against MCF-7 and HCT-116 cell line [16]. UV-Vis spectroscopy indicated that the complexes exhibited good binding capacity with CT-DNA. In another report, a series of Ru (II) arene complexes were synthesized with the arene group varying between *p*-cymene, phenoxyethanol and benzene. Because of the inherent biological activity of benzimidazole, 2-pyridin-benzimidazole and 2-phenyl-benzimidazole based ligands were used. The complexes were found to be cytotoxic and its mechanism was attributed to the dual mode of binding to CT-DNA via covalent interaction of ruthenium to guanine nucleobase and intercalation of the aromatic rings between adjacent base pairs of DNA, with the *p*-cymene complexes showing higher activity.

In a report by Pettinari *et al.*, several ruthenium(II) arene complexes having PTA and curcumin as ligands were synthesized and characterized followed by investigating their antitumour activity. The RAPTA complexes exhibited good solubility and cytotoxicity with IC<sub>50</sub> values being less than 1 μM. The curcumin behaves as a potential leaving group and PTA improved the biological activity [22].

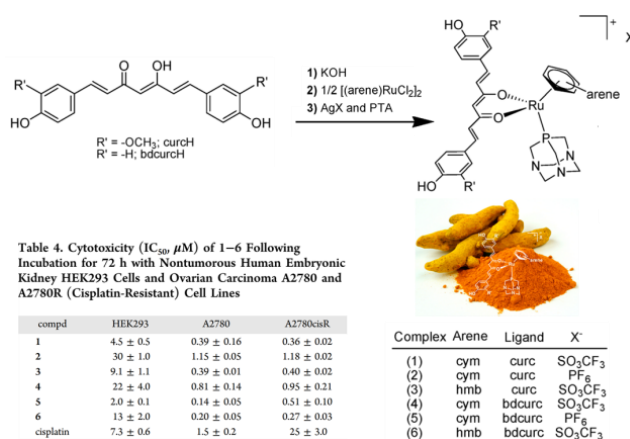


**Figure 2.2:** Synthesis of RAPTA complexes using curcumin as the leaving group. Reproduced with permission from ref. 22. Copyright 2014 American Chemical Society

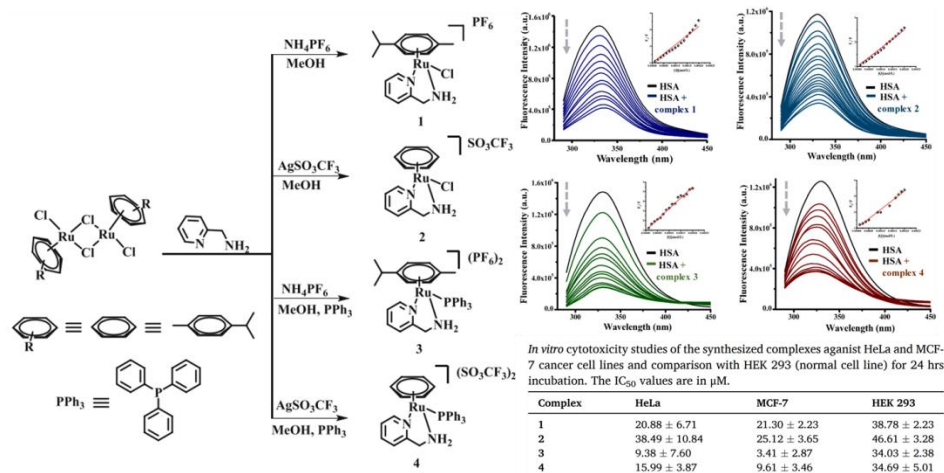


**Figure 2.3:** Synthesis of Ru(II) arene complexes with varying co-ligands and their effect on cytotoxicity. Reproduced with permission from ref. 23. Copyright 2021 Elsevier.

In another report by Praggi *et al.*, four ruthenium(II) arene complexes with piano-stool geometry and varying co-ligands (Cl/PPh<sub>3</sub>) and

counter anions ( $\text{PF}_6^-/\text{SO}_3\text{CF}_3^-$ ) and having 2-aminomethyl pyridine as the bidentate ligand was synthesized and their anticancer activity was studied. Upon addition of these complexes to HSA, significant quenching of fluorescence intensity was observed indicating good binding of the complexes with the protein. Complex 3 having the *p*-cymene moiety and triphenylphosphine group exhibited maximum binding interaction with HSA due to increased hydrophobicity. UV-Vis study was conducted to know how the complexes bind with DNA. Upon adding CT-DNA to a fixed concentration of complex hyperchromism was observed indicating the groove binding mode of the complexes. Fluorescence quenching studies using DAPI also revealed the same result as quenching of fluorescence was observed with increasing amount of complex. The complexes replace DAPI from the DNA thereby confirming its groove binding nature. The complexes were also efficient in catalysing the oxidation of NADH, leading to generation of reactive oxygen species which causes oxidative damage to cells thereby leading to cell death. This hydride transfer from NADH to Ru(II) occurs via ring slippage mechanism [23]. All the complexes exhibited cytotoxicity against MCF7 and HeLa cells and their  $\text{IC}_{50}$  values were much higher for normal cell line indicating their specificity towards cancer cells [23].

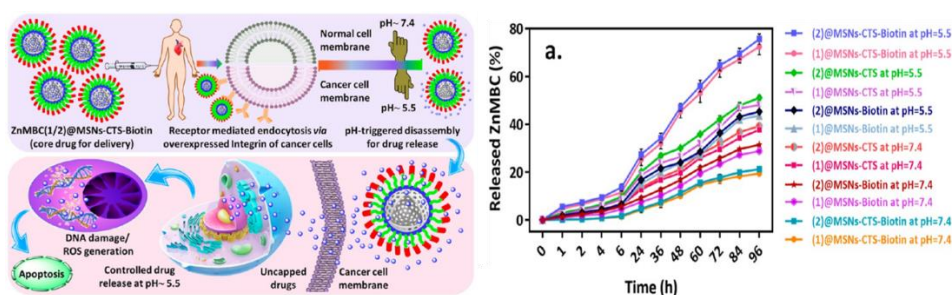


**Figure 2.4:** Chitosan-Biotin conjugated MSNs for targeted drug delivery. Reproduced with permission from ref. 24. Copyright 2022 American Chemical Society

There are reports where the anticancer activity of cisplatin and transplatin was found to be enhanced upon loading them on mesoporous silica nanoparticles [24]. In a previously reported paper

Chitosan-Biotin conjugated mesoporous silica nanoparticles were used to selectively target cancer cells. The MSNs were loaded with organometallic zinc complexes and wrapped with chitosan conjugated with biotin, as biotin helps in the selective cellular uptake by cancer cells. The drug loaded nanoparticles showed enhanced cytotoxicity compared to free drugs. The drug release profile was also studied in neutral and acidic pH and the drug release was found to be much greater in malignant cells than in non- malignant cells. The interaction between drug and silica matrix weakens at lower pH causing release of drugs [25].

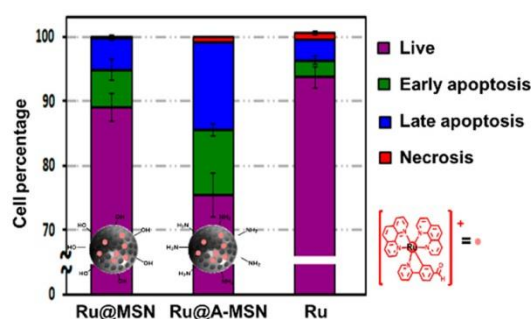


**Figure 2.5:** Improved cytotoxicity upon loading Ru(II) complex on A-MSNs. Reproduced with permission from ref. 21. Copyright 2020 American Chemical Society

In another recent report by Carmona *et al.* an octahedral ruthenium(II) complex has been encapsulated in different types of mesoporous silica nanoparticles and their cytotoxicity was investigated. The complex  $[\text{Ru}(\text{ppy-CHO})(\text{phen})_2]\text{PF}_6$  when encapsulated on MSN and amine functionalized MSNs (A-MSNs) induced apoptosis and necrosis and also affected the cell cycle progression and the results obtained were much better when compared to free bare drug only. The drug loaded amino functionalized MSNs exhibited very high cytotoxicity against U87 glioblastoma cancer cell lines. The amine functionalized MSN showed better cellular uptake than pristine MSN due to interaction between the negatively charged phospholipids and positively charged surface of the nanoparticles. Also, the interaction of the ruthenium complex with silica matrix was studied at two different pH values (pH-

7.4 and pH-5.4 representing the normal cell and cancer cell environment respectively) [21].

Inspired by these reports and findings, three Ru(II) complexes have been designed and synthesized in this work where a fluorescent benzimidazole containing bidentate chelating ligand with nitrogen and oxygen as the donor atoms has been incorporated. Different co-ligands like chloride, a labile group, PPh<sub>3</sub> (triphenylphosphine), a hydrophobic moiety and PTA (1,3,5-triaza-7-phosphatrimethylene-3,3,1,1] decane, water soluble ligand have been used to study the effect of co-ligands on cytotoxicity. The synthesized complexes were then studied for their anticancer activity and the one possessing the highest cytotoxicity was loaded on amine functionalized mesoporous silica nanoparticles to study whether these drug delivery vehicles can enhance the cytotoxic activity.

## *Chapter 3*

### **EXPERIMENTAL SECTION**

#### **3.1 Reagents and Chemicals**

The chemicals used in the experiment were bought from Alfa Aesar, Avra and Sigma Aldrich, India and no more purification was done before use. Chemicals used for biological experiments like (3-(4,5-dimethylthiazol-2-yl)-2,5-diphenyltetrazolium bromide (MTT), PBS buffer and media were obtained from Himedia Chemical, India.

#### **3.2 Methods and Instrumentation**

For recording ESI-MS spectra, mass spectrometer from Bruker-Daltonics, microTOF-Q II was utilized. AVANCE NEO500 Ascend Bruker BioSpin international AG equipment with TMS as the standard reference was used to record the proton  $^1\text{H}$  NMR and  $^{13}\text{C}$  NMR spectra. Fourier Transfer Infrared (FTIR) spectra were recorded on a Bruker Tensor 27 FTIR spectrometer (range: 4000 to 500  $\text{cm}^{-1}$ ). Fluoromax-4 spectrofluorometer (HORIBA Jobin Yvon, model FM-100) was used to record the fluorescence spectra and the samples were placed in a quartz cuvette of path length 1 cm at  $25.0 \pm 0.2$  °C. For studying absorption spectra PerkinElmer UV/Vis/NIR spectrometer in a quartz cuvette (1 cm  $\times$  1cm) was used. Fluoview FV100 (OLYMPUS, 449 Tokyo, Japan) confocal microscope was used for imaging in the staining assays. Supra55 Zeiss field emission scanning electron microscopy (FE-SEM) was used to capture the morphological image of the nanoparticles. For the porosity parameters Quantachrome, Autosorb iQ2 Brunauer-Emmett-Teller (BET) surface area analyzer was used. PXRD was recorded on Empyrean, Malvern Panalytical, with  $\text{Cu-K}_\alpha$  radiation. TGA experiments were done using Mettler Toledo Thermal Analyser with heating rate of 10 °C.

### 3.3 Synthesis of Ruthenium Dimer, Ligand and Metal Complexes

#### *3.3.1 Synthesis of Ruthenium Dimer – [Ru(*p*-cym)Cl<sub>2</sub>]<sub>2</sub>*

The ruthenium *p*-cymene dimer was synthesized by dissolving 0.5 g of hydrated ruthenium trichloride in 25 mL of ethanol and stirring for fifteen minutes. To it 3.5 mL of phellandrene was added and refluxed for six hours at 85 °C. After that the solution was allowed to cool and was made concentrated by evaporating a part of the solvent. The concentrated solution was then kept in fridge for overnight which lead to precipitate formation. The precipitate was then filtered followed by washing of the residue using hexane to obtain reddish brown microcrystalline product (0.58 g). Yield- 79%

#### *3.3.2 Synthesis of Ligand (HL)*

The ligand **HL** was synthesized by dissolving 0.14 g (1 mmol) of 2,4-dihydroxy benzaldehyde, 0.16 g (1 mmol) of 2,3- diamionaphthalene and 0.11 g (slight excess) of sodium bisulphite in N, N-dimethylformamide (DMF) solvent and stirring it under reflux condition for twelve hours at 120 °C. Then the solution was cooled down and ice cold water was added which lead to precipitate formation. The precipitate was then filtered and washed using MQ-H<sub>2</sub>O. After drying a pale yellow coloured product was obtained (0.20 g). Yield- 74%

#### *3.3.3 Synthesis of [Ru( $\eta^6$ -*p*-cym)(L)Cl] (C1)*

The complex **C1** was synthesized by first dissolving 0.1 g (0.16 mmol) of ruthenium *p*-cymene dimer in 10 mL methanol and then adding a methanolic solution (10 mL) of the ligand **HL** (0.09 g, 0.32 mmol) to it. The reaction mixture was then made to stir at normal room temperature for six hours. The solution was then filtered followed by evaporating the solvent. Recrystallized product was obtained from methanolic solution by slow evaporation (0.13 g). Yield- 74%

### 3.3.4 Synthesis of $[Ru(\eta^6\text{-}p\text{-cym})(L)PPh_3]PF_6$ (C2)

Complex **C2** was synthesized by dissolving 0.1 g (0.16 mmol) of ruthenium *p*-cymene dimer in methanol (10 mL) and then adding methanolic solution (10 mL) of ligand **HL** (0.09 g, 0.32 mmol) to it. The reaction mixture was stirred at room temperature for six hours. This was followed by addition of a methanolic solution of 0.08 g (0.32 mmol) triphenylphosphine and agitating the reaction mixture again for twelve hours at room temperature. Then 0.05 g (0.32 mmol) of ammonium hexafluorophosphate dissolved in methanol was added as counter anion and further stirred for two hours more. The solution was then filtered followed by evaporating the solvent using rotary evaporator to yield a brownish compound. The product was recrystallized using dichloromethane by slow evaporation (0.19 g). Yield- 65%

### 3.3.5 Synthesis of $[Ru(\eta^6\text{-}p\text{-cym})(L)(PTA)]PF_6$ (C3)

Complex **C3** was synthesized by dissolving 0.1 g (0.16 mmol) of ruthenium *p*-cymene dimer in methanol (10 mL) and then adding methanolic solution (10 mL) of ligand **HL** (0.09 g, 0.32 mmol) to it. The reaction mixture was then stirred for six hours at normal room temperature. This was followed by adding a methanolic solution of 0.05 g (0.32 mmol) of 1,3,5-triaza-7-phosphaadamantane and stirring the reaction mixture again for twelve hours at room temperature. Then 0.05 g of (0.32 mmol) ammonium hexafluorophosphate was dissolved in methanol and added to it. Stirring was continued for two hours more. The solution was then filtered followed by evaporating the solvent using rotary evaporator to yield a deep brown coloured compound. The product was recrystallized from methanolic solution by slow evaporation (0.16 g). Yield- 61%

### **3.4 Synthesis of MSNs, A-MSNs and C2@A-MSNs**

#### **3.4.1 Synthesis of MSNs**

1 g of CTAB (Cetyltrimethyl ammonium bromide) and 280 mg of NaOH was dissolved in 480 mL of distilled water and the reaction mixture was heated at 80 °C with vigorous stirring for thirty minutes. To it 5 g of TEOS (Tetraethyl orthosilicate) was added and was further heated for two hours. The white precipitate obtained was washed thrice with MQ-H<sub>2</sub>O and twice with methanol and vacuum dried. The CTAB was removed by heating the synthesized material dissolved in 100 mL methanol and 0.75 mL concentrated HCl for six hours at 50 °C. The solid product was filtered and vacuum dried to obtain white coloured product (0.96 g) [25].

#### **3.4.2 Synthesis of Amine functionalized MSNs (A-MSNs)**

Functionalization of MSN was done by suspending 1 g of MSN in 30 mL toluene and adding 0.63 mL (0.6 g, 2.7 mmol) APTES to it. The reaction mixture was refluxed for eight hours at 110 °C and the nanoparticles were recovered by centrifugation. The nanoparticles were washed with ethanol and deionized water and vacuum dried to obtain cream coloured product (0.80 g).

#### **3.4.3 Loading of C2 on A-MSNs**

100 mg of amino functionalized MSN was added to methanolic solution of C2 (100 mg dissolved in 10 mL) and the reaction mixture was stirred for twenty-four hours in dark. The drug loaded nanoparticles were collected by centrifugation, washed with MQ water and dried under vacuum to obtain pale yellow colour product. The loading capacity (LC) of C2 in the nanomaterials was determined by weight with following formula:

For weight method:  $LC = (m_1 - m_0) / m_1$  ..... (1)

Herein,  $m_0$  and  $m_1$  mean the weight of A-MSNs before and after loading process.

### **3.5 Stability Study**

To check the stability of the complexes in biological medium stock solution of 1mM/2mL was made in DMSO. The UV-Vis spectrum was recorded in PBS buffer after suitable dilution at time intervals of 0 hour, 6 hours, 12 hours and 24 hours. Since the tumour environment is acidic in nature and the drug carrier is expected to release the loaded drug in lower pH the complex **C2** was checked for its stability in acidic pH. The absorption spectrum was recorded after every twenty-four hours. For this 100  $\mu$ L of stock solution of **C2** was dissolved in PBS buffer having an acidic pH of 5.4 mimicking the acidic environment of cancer cells.

### **3.6 Lipophilicity Study**

The lipophilic behaviour of the complexes was studied using shake-flask method [26]. To determine the extinction coefficient of the synthesized complexes, absorbance was recorded for five different concentrations (5  $\mu$ M, 10  $\mu$ M, 20  $\mu$ M, 40  $\mu$ M, 60  $\mu$ M). The slope obtained from the plot of absorbance vs concentration gave the value of extinction coefficient. To determine the partition coefficient of the synthesized complexes, 5 mg of each complex was dissolved in 10 mL of n-octanol and 10 ml of water-DMSO (2:1) mixture. The resulting mixture was shaken for fifteen minutes and allowed to equilibrate for twenty-four hours in a separating funnel. This lead to the separation of the two phases, the organic phase of n-octanol being at the top and the aqueous phase of water-DMSO being at the bottom. The two phases were collected separately and their absorbance was recorded. Using the extinction coefficient and the absorbance, the concentration of the complexes in the two phases were calculated using Beer Lambert Law and the partition coefficient was calculated using Equation 1.

$$P_{O/W} = \frac{\text{Concentration in octanol}}{\text{Concentration in water}} \quad \dots (1)$$

### **3.7 Protein Binding Study**

To determine whether the synthesized complexes interact with albumin proteins (BSA and HSA), tryptophan quenching experiments were performed. BSA/HSA solution was excited at a wavelength of 280 nm and the slit width was kept constant throughout the experiment. Decrease in fluorescence intensity of tryptophan at 346 nm was measured by increasing the concentration of the complexes. NaCl/ Tris HCl buffer (50mM/ 5 mM buffer, pH 7.4) solution was used to prepare stock solution of BSA/HSA of concentration 10  $\mu$ M and kept at 4  $^{\circ}$ C for future use. Stock solutions of 1 mM of the complexes were prepared in DMSO. For fluorometric titration, the fluorescence intensity was measured as blank using 2 mL of protein solution. Each time, to the protein solution, 10  $\mu$ L of the complexes were added and the emission spectrum was taken. To quantify fluorescence quenching, stock solutions upto 80  $\mu$ L was added. The quenching of fluorescence was further quantified using Stern Volmer equation (Equation 2).

$$\frac{F_0}{F} = 1 + K_q\tau_0 [Q] = 1 + K_{SV} [Q] \quad \dots (2)$$

where  $F_0$  stands for fluorescence intensity when there is no quencher (metal complex) and  $F$  stands for the same when there is a quencher molecule,  $K_q$  represents the bimolecular quenching rate constant,  $\tau_0$  is the fluorophore's average lifespan when there is no quencher, and  $[Q]$  is the concentration of the quencher.  $K_{SV}$  in  $M^{-1}$  stands for the Stern–Volmer quenching constant. The following formula is used to compute  $K_a$  and  $n$  which represents the binding constant and the number of complexes bound to BSA/HSA respectively [23].

$$\log \left[ \frac{(F_0 - F)}{F} \right] = \log K_a + n \log [Q] \quad \dots (3)$$

## **3.8 Nucleic acid Binding Study**

### **3.8.1 Absorption Spectroscopy**

To investigate the binding of the synthesized complexes with nucleic acids, UV-Vis spectroscopy was performed. 1 mM stock solution was obtained by desolving required amount of the synthesized complexes in DMSO. DNA solution was prepared in NaCl/ Tris HCl buffer (50mM/ 5 mM buffer, pH 7.4). The absorption spectra of the synthesized complexes/ ligand were recorded after suitable dilution. To it 10  $\mu$ L of CT-DNA solution was added each time and the absorbance was monitored. The titration was performed up to 100  $\mu$ L of CT-DNA [17].

### **3.8.2 Emission Spectroscopy**

To confirm the mode of binding to DNA, competitive fluorometric displacement assay was performed using ethidium bromide as the intercalating agent. Stock solution of 1mg/ mL ethidium bromide was prepared in Tris HCl buffer and stock solutions of 1 mM of the complexes were prepared in DMSO. The excitation was done at 518 nm, and the slit width was kept constant throughout the experiment. The fluorescence intensity of 110  $\mu$ L of CT-DNA and 20  $\mu$ L of ethidium bromide in Tris HCl buffer solution was taken as blank. To it 10  $\mu$ L of the synthesized complexes/ ligand was added and the fluorescence intensity was measured each time. The change in fluorescence intensity at 609 nm was monitored and the quenching parameters were quantified using Stern Volmer equation (Equation 2) and Scatchard equation (Equation 3). Similar protocol was performed to study the binding of the complexes with RNA [17].

## **3.9 Drug Release Study**

The drug release study was done in PBS buffer at two different pH values. An acidic pH of 5.4 was used to mimic the cancer cell environment and a neutral pH of 7.4 was used to mimic the normal cell environment. 10 mg of **C2@A-MSNs** was dissolved in 10 mL of

DMSO/PBS buffer solutions of pH 5.4 and pH 7.4 and the reaction mixture was stirred for ninety-six hours. 500  $\mu\text{L}$  of the reaction mixture was taken out at different time intervals and UV-Vis spectrum was recorded for the supernatant solution. Each time 500  $\mu\text{L}$  was taken out, equal amount of fresh PBS buffer solution of corresponding pH was added to maintain the constancy of total volume. From the UV-Vis absorption spectra data the drug release profile was plotted [25].

### **3.10 Cell Viability Assay**

The cytotoxicity of the synthesized complexes was investigated using MTT assay. MTT [3-(4, 5-dimethylthiazol-2-yl)-2, 5-diphenyltetrazoliumbromide] is a yellow coloured tetrazolium salt which is reduced to formazan a purple coloured insoluble product in the presence of mitochondrial reductase an enzyme present only in live cells. The cell viability assay was performed on HeLa and DU145 cancer cells and HEK 293 normal cells. A 96-well plate was seeded with  $5 \times 10^4$  cells/well and allowed to attach and grow for twenty-four hours in  $\text{CO}_2$  environment. Stock solution of 2 mM was prepared by dissolving the ruthenium complexes in DMSO. The cells were treated with the synthesized complexes, ligand and cisplatin with concentration varying from 0.25 to 100  $\mu\text{M}$  and were then allowed to incubate for twenty-four hours. After that, the cell culture medium was discarded followed by addition of 10  $\mu\text{L}$  of MTT solution to each well. The cells were then incubated in dark for four hours followed by discarding MTT and adding 100  $\mu\text{L}$  of DMSO to solubilize the purple product. The experiment was performed in triplicates and the medium without any treatment was considered as the control. Using a microplate reader, the absorbance at 570 nm was recorded and percentage cell viability was calculated using equation 4.

$$\% \text{ cell viability} = \frac{\text{OD value of treated cells}}{\text{OD value of untreated cells (control)}} \times 100 \quad \dots (4)$$

The concentration at which 50 % of cells die ( $IC_{50}$ ) was determined from the linear regression curve of absorbance vs concentration using Prism GraphPad software. Each well was triplicated and each experiment repeated at least three times.  $IC_{50}$  values are quoted as mean  $\pm$  SEM [17].

### **3.11 Apoptosis Study using Dual Staining Method**

To study the morphological changes during apoptosis, dual staining assay was performed using Acridine Orange (AO) and Ethidium Bromide (EtBr) dyes. In a 6 well plate HeLa cells were treated with the  $IC_{50}$  values of the free complexes as well as the loaded complex and were allowed to incubate for twenty-four hours. After that, AO ( $5 \mu\text{g mL}^{-1}$ ) and EtBr ( $3 \mu\text{g mL}^{-1}$ ) dyes were used to stain the treated cells and left to incubate for another ten minutes at  $37^\circ\text{C}$ . After sixty minutes the cells were washed thrice with PBS and using Fluoview FV100 (OLYMPUS, Tokyo, Japan) confocal microscope of appropriate filters (EtBr and AO having excitation wavelengths 301 and 502 nm and an emission wavelength of 603 and 525 nm, respectively) fluorescence was viewed [17].

### **3.12 ROS Generation- DCFH-DA Staining**

Ruthenium complexes are known for their ability to generate ROS which can be one of the reasons for cell death. Thus, to investigate whether the synthesized complexes are potent of generating ROS, DCFH-DA staining assay was performed. In a 6 well tissue culture plate, HeLa cells were seeded and left to incubate for twenty-four hours under  $\text{CO}_2$  environment. After that the cells were treated with  $IC_{50}$  values of the synthesized complexes and the cells untreated were considered as control. The treated cells were further incubated for twenty-four hours and then washed with PBS twice.  $10 \mu\text{M}$  of DCFH-DA dye was used to stain the treated cells and left to incubate for thirty minutes at  $37^\circ\text{C}$ . This was followed by washing the cells with PBS

twice and then adding DMEM to each well. The green cells were then photographed using confocal microscopy [23].

### **3.13 Metastasis Inhibition**

To study the antimetastatic property of the synthesized complexes, wound healing assay was performed. A 6-well plate was seeded with 2 mL of media and HeLa cancer cells ( $1.5 \times 10^6$  per well) and was allowed to attach and grow to form a confluent monolayer. A horizontal line was drawn on each well of the plate which passed through the centre of the bottom and 10  $\mu$ L pipette tips were used to create wounds perpendicular to the drawn lines. PBS (pH-7.4) was used to remove and wash the detached cells. The cells were incubated at 37 °C after addition of the complexes in DMEM with 1% FBS under 5% CO<sub>2</sub> environment for imaging. For suppression of cell proliferation, DMEM with 1% FBS was used. At t=0 and 24 h images were taken at same position of each well. The same procedure was repeated three times [17].

## Chapter 4

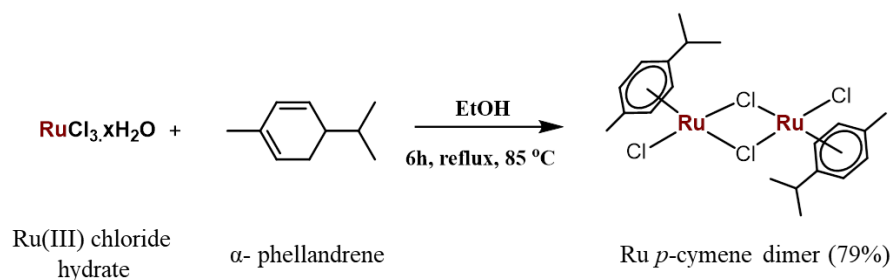
# RESULTS AND DISCUSSION

### 4.1 Structure and Synthesis

Three piano stool Ru(II) arene complexes have been synthesized and characterized. The complexes have pseudo-octahedral geometry with the arene moiety occupying three coordination sites and the bidentate chelating ligand **HL** occupying two of the other coordination sites in its uninegative form. N and O act as the donor sites for the chelating ligand. The ligand at the sixth position was varied between chloride, PPh<sub>3</sub> and PTA. PPh<sub>3</sub> was chosen because of its hydrophobic nature which is expected to facilitate the transportation of the drug through the cell membrane while PTA because of its water solubility nature is expected to increase the aqueous solubility of the drug. As counteranions, hexafluorophosphate was employed where NH<sub>4</sub>PF<sub>6</sub> is utilized as precursor. **C1** was synthesized by the reaction of the Ru dimer and ligand (**HL**). The chloride ligand was substituted by PPh<sub>3</sub> or PTA followed by the addition of necessary counteranions to obtain complex **C2** and **C3**. **MSN** was synthesized using the surfactant CTAB and silica precursor TEOS. APTES was used to functionalize the surface of **MSN** with NH<sub>2</sub> groups and the complex **C2** was loaded on it.

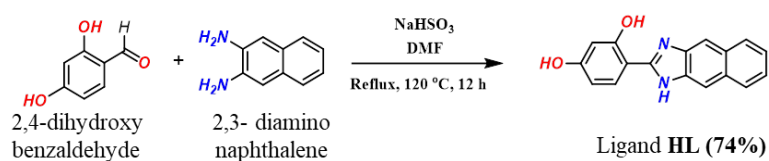
### 4.2 Reaction Schemes

#### *4.2.1 Synthesis of Ruthenium *p*-cymene dimer*



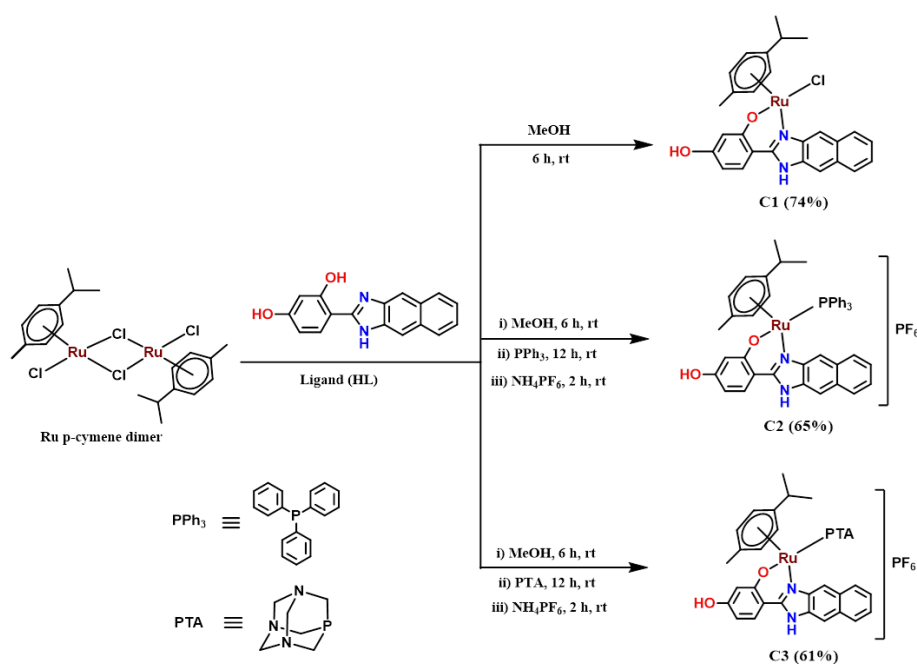
*Scheme 4.1: Reaction scheme for the synthesis of dimer*

#### 4.2.2 Synthesis of Ligand (HL)



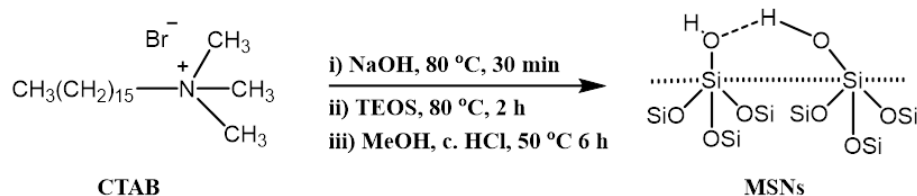
**Scheme 4.2:** Reaction scheme for the synthesis of ligand HL

#### 4.2.3 Synthesis of Complexes C1, C2 and C3

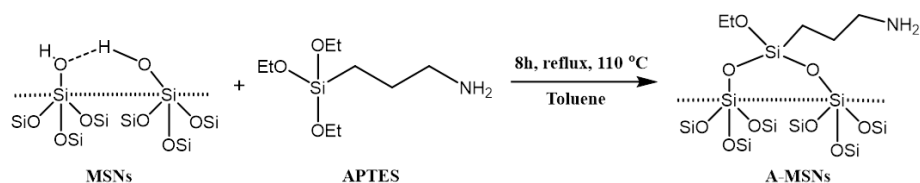


**Scheme 4.3:** Reaction scheme for the syntheses of complexes C1, C2, C3

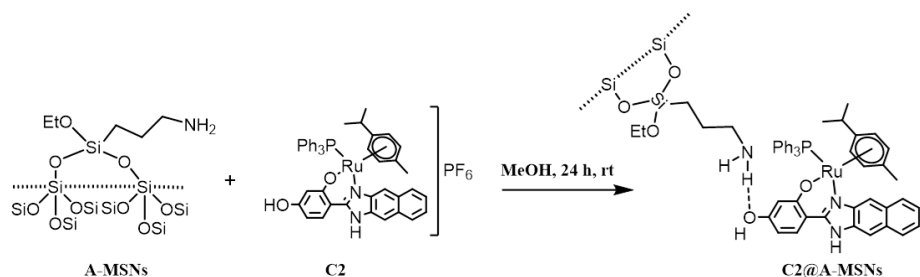
#### 4.2.4 Synthesis of MSNs and Amino-functionalized MSNs



**Scheme 4.4:** Reaction scheme for the synthesis of MSNs



**Scheme 4.5:** Reaction scheme for amine functionalization of **MSNs**



**Scheme 4.6:** Reaction scheme for loading of **C2** on **A-MSNs**

## **4.3 Characterization**

### ***4.3.1 Mass Spectra and Elemental Analysis***

All the synthesized compounds were characterized by ESI-MS spectra. The ligand **HL** shows a base peak at  $m/z = 277.1165$  corresponding to  $[\text{H}_2\text{L}]^+$  while for complex **C1** the peak is obtained at  $m/z = 511.0641$  due to the  $[\text{RuL}(\text{p-cym})]^+$  fragment after losing one chloride ion. For complex **C2** the peak is obtained at  $m/z = 773.1202$  corresponding to the cationic complex  $[\text{RuL}(\text{p-cym})\text{PPh}_3]^+$  and for complex **C3** the peak at  $m/z = 668.1340$  in the spectra corresponds to the cationic complex  $[\text{RuL}(\text{p-cym})\text{PTA}]^+$ .

Elemental analysis for **HL** (%): Calc. for  $\text{C}_{14}\text{H}_{12}\text{N}_2\text{O}_2$ : C, 73.90; H, 4.38; N, 10.14; Found: C, 74.20; H, 4.56; N, 10.98.

Elemental analysis for **C1** (%): Calc. for  $\text{C}_{27}\text{H}_{25}\text{N}_2\text{O}_2\text{Ru}$ : C, 59.39; H, 4.62; N, 5.13; Found: C, 60.20; H, 4.96; N, 5.87.

Elemental analysis for **C2** (%): Calc. for  $\text{C}_{45}\text{H}_{40}\text{F}_6\text{N}_2\text{O}_2\text{P}_2\text{Ru}$ : C, 58.89; H, 4.39; N, 3.05; Found: C, 59.40; H, 5.06; N, 3.76.

Elemental analysis for **C3** (%): Calc. for  $\text{C}_{33}\text{H}_{37}\text{F}_6\text{N}_5\text{O}_2\text{P}_2\text{Ru}$ : C, 48.77; H, 4.59; N, 8.62; Found: C, 49.43; H, 5.36; N, 9.36.

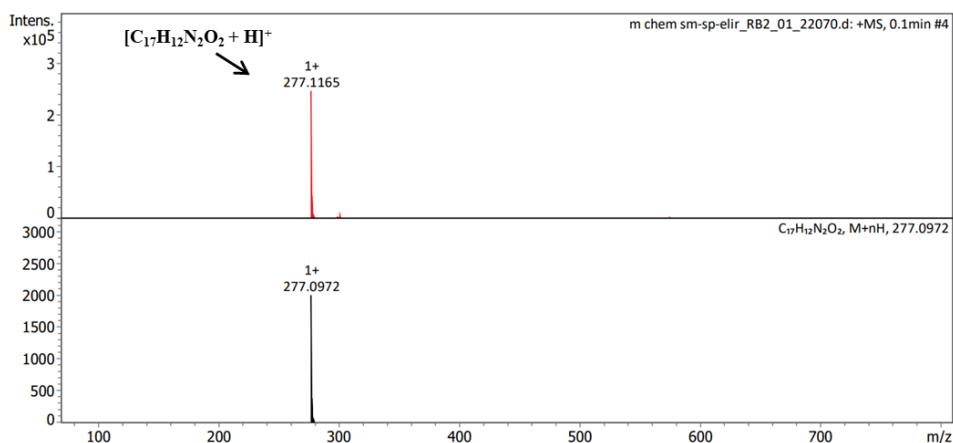


**Figure 4.1:** Mass spectrum of ligand **HL**; ESI-MS ( $m/z$ )  $C_{17}H_{12}N_2O_2$ :  
 Calculated for  $[C_{17}H_{12}N_2O_2 + H]^+$ : 277.09; Found: 277.1165

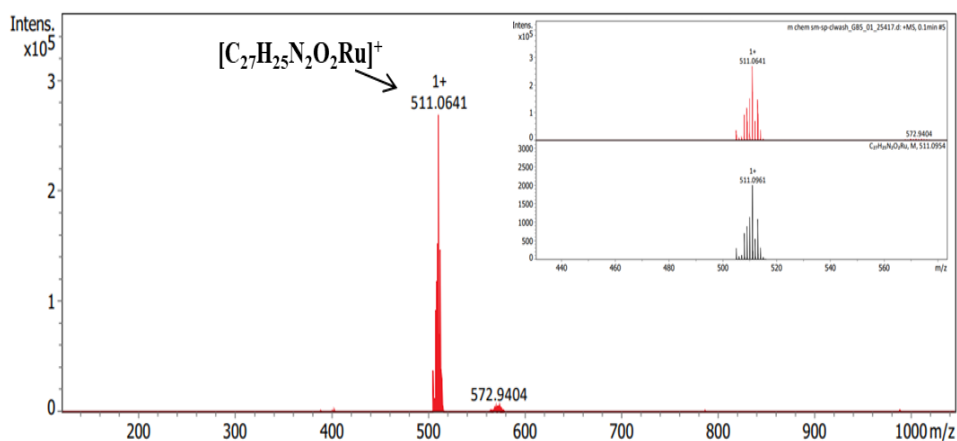


**Figure 4.2:** Mass spectrum of complex **CI**; ESI-MS ( $m/z$ )  
 $C_{27}H_{25}N_2O_2ClRu$ : Calculated for  $[C_{27}H_{25}N_2O_2Ru]^+$ : 511.0961; Found:  
 511.0641

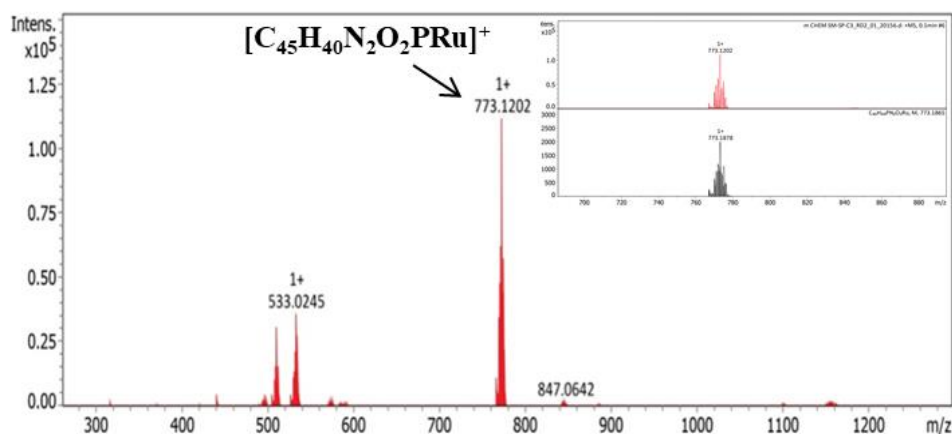


**Figure 4.3:** Mass spectrum of complex **C2**; ESI-MS ( $m/z$ )  
 $C_{45}H_{40}N_2O_2PRu$ : Calculated for  $[C_{45}H_{40}N_2O_2PRu]^+$ : 773.1878;  
 Found: 773.1202

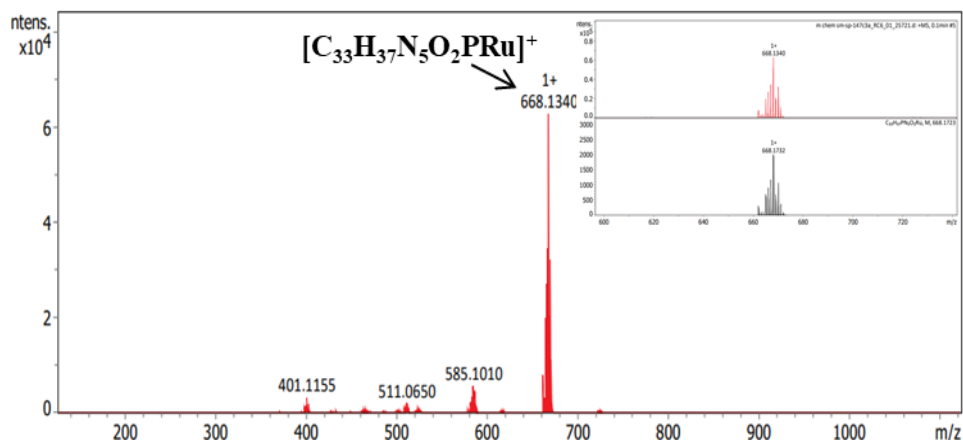


**Figure 4.4:** Mass spectrum of complex **C3**; ESI-MS ( $m/z$ )  
 $C_{33}H_{37}N_5O_2PRu$ : Calculated for  $[C_{33}H_{37}N_5O_2PRu]^+$ : 668.1732;  
 Found: 668.1340

### 4.3.2 NMR Spectra

NMR spectroscopic data of complex **C1**, **C2**, **C3** and ligand (**HL**) further justified the predicted structures. The NMR spectra were recorded with samples dissolved in DMSO- $d_6$ .  $^1H$  NMR peaks in the  $\delta$  5.25–6.05 ppm region corresponds to *p*-cymene aromatic protons while the aromatic proton peaks of the ligand (**HL**) appear at  $\delta$  8.27-6.45. The peaks at  $\delta$  2.8, 1.7-2.09, 0.9-1.2 ppm are due to the methyl and isopropyl groups of *p*-cymene ring. The highly deshielded broad peaks after 10 ppm correspond to OH and NH proton [26]. The PTA protons are observed in the region  $\delta$  4.73-4.26 ppm and the peaks for  $PPh_3$  aromatic ring protons appear in the region  $\delta$  7.44-7.15 ppm [27].

#### 4.3.2.1 NMR Spectra of Ligand (HL)

$^1H$  NMR (500.13 MHz, 298 K, DMSO- $d_6$ )  $\delta$ , ppm: 13.02, 10.23 [s, H of N-H and O-H], 8.10, 8.02, 7.96, 7.41, 6.53, 6.48 [ligand aromatic protons].  $^{13}C$  NMR (125 MHz, DMSO- $d_6$ )  $\delta$ , ppm: 156.5 [C of NH-C=N], 161.2, 162.4 [C of C-OH], 130.5, 128.9, 128.2, 124.2, 108.4, 104.0, 103.3, [C of ligand].

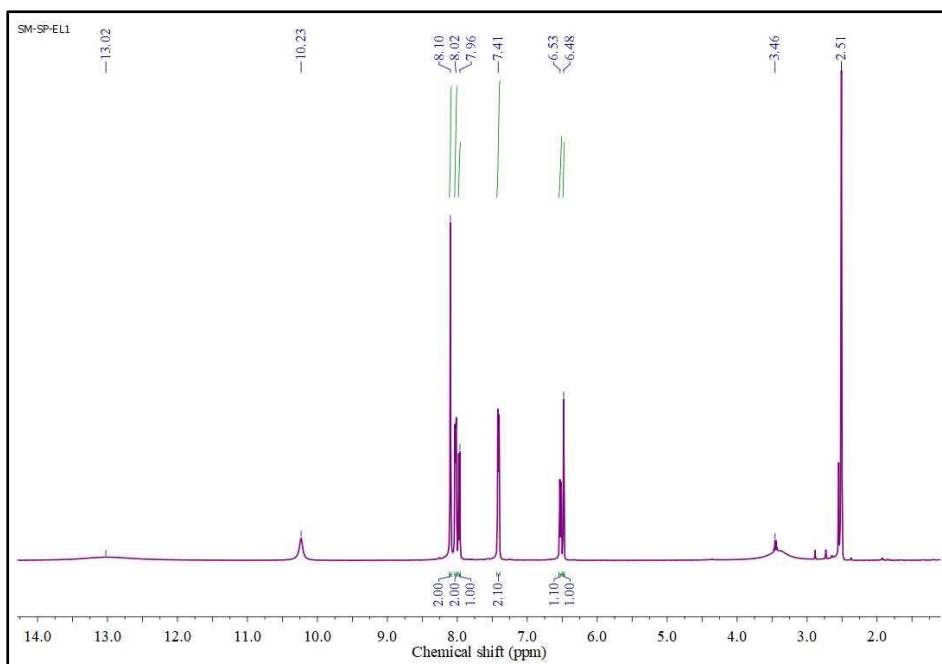


**Figure 4.5:**  $^1\text{H}$  NMR spectrum of ligand **HL**

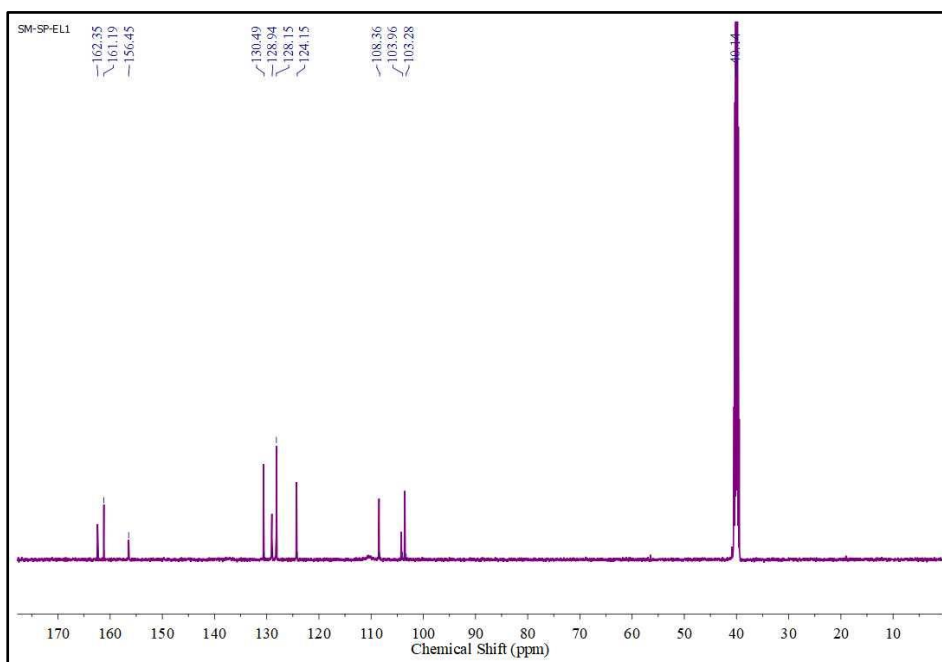


**Figure 4.6:**  $^{13}\text{C}$  NMR spectrum of ligand **HL**

#### 4.3.2.2 NMR Spectra of Complex **C1**

$^1\text{H}$  NMR (500.13 MHz, 298 K, DMSO- $d_6$ )  $\delta$ , ppm: 13.21, 10.41 [s, 1H, H of N-H & O-H], 8.14-6.54 [ligand aromatic protons], 5.81-5.78 [*p*-cymene aromatic protons], 2.83 [m, 1H, CH(CH $_3$ ) $_2$ ], 2.09 [s, 3H, CH of C $_6$ H $_4$ CH $_3$ ], 1.18 [d, 6H, CH of C(CH $_3$ ) $_2$ ].  $^{13}\text{C}$  NMR (125 MHz,

DMSO-d<sub>6</sub>)  $\delta$ , ppm: 155.1 [C of NH-C=N], 163.0, 161.1 [C of C-OH], 138.7, 130.8, 129.7, 128.2, 124.6, 108.8, 106.8, 103.5, 100.6 [C of ligand], 86.8, 86.0 [C of *p*-cymene ], 30.4 [CH of *p*-cymene], 21.7 [C(CH<sub>3</sub>)<sub>2</sub> of *p*-cymene], 18.3 [CH<sub>3</sub> of *p*-cymene].

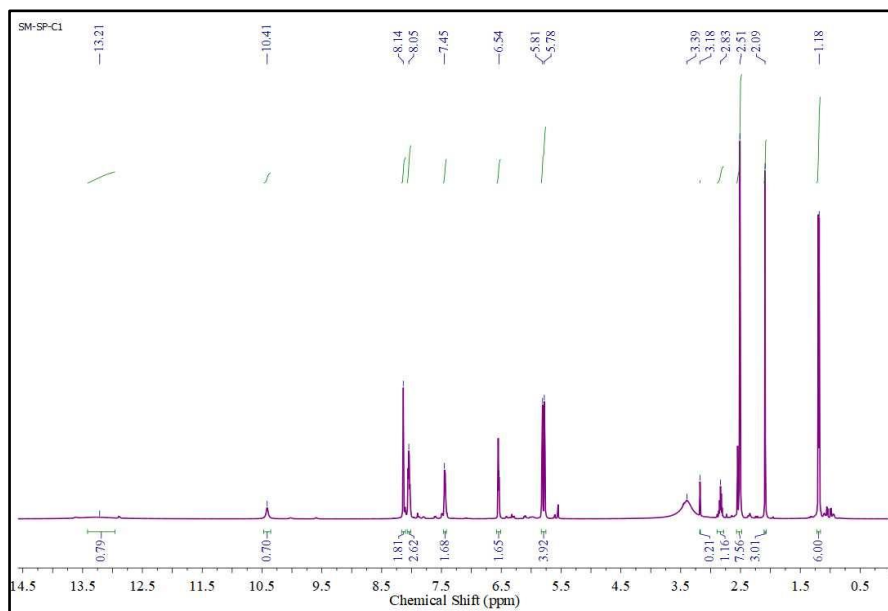


**Figure 4.7:** <sup>1</sup>H NMR spectrum of complex C1

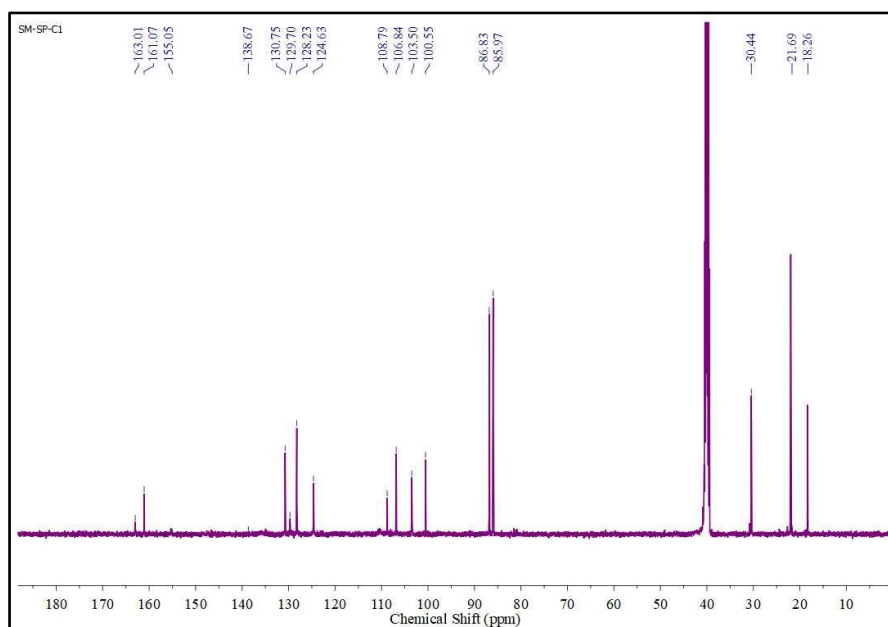


**Figure 4.8:** <sup>13</sup>C NMR spectrum of complex C1

### 4.3.2.3 NMR Spectra of Complex C2

$^1\text{H}$  NMR (500.13 MHz, 298 K, DMSO- $d_6$ )  $\delta$ , ppm: 14.13, 10.85 [s, 1H, H of N-H & O-H], 8.26-6.61 [ligand aromatic protons], 5.30-5.25 [*p*-cymene aromatic protons], 2.51 [m, 1H, CH(CH $_3$ ) $_2$ ], 1.77 [s, 3H, CH of C $_6$ H $_4$ CH $_3$ ], 0.95 [d, 6H, CH of C(CH $_3$ ) $_2$ ].  $^{13}\text{C}$  NMR (125 MHz, DMSO- $d_6$ )  $\delta$ , ppm: 153.3 [C of NH-C=N], 162.4, 160.8 [C of C-OH], 133.5, 133.0, 132.1 [C of PPh $_3$ ], 134.6, 130.5, 129.3, 128.4, 124.8, 108.9, 103.4 [C of ligand], 89.7, 87.0 [C of *p*-cymene], 30.0 [CH of *p*-cymene], 21.8 [C(CH $_3$ ) $_2$  of *p*-cymene], 17.7 [CH $_3$  of *p*-cymene ring].  $^{31}\text{P}$  NMR (126 MHz, DMSO- $d_6$ )  $\delta$ , ppm: 23.93 [s, PPh $_3$ ], -144.74 [sept, PF $_6$ ].

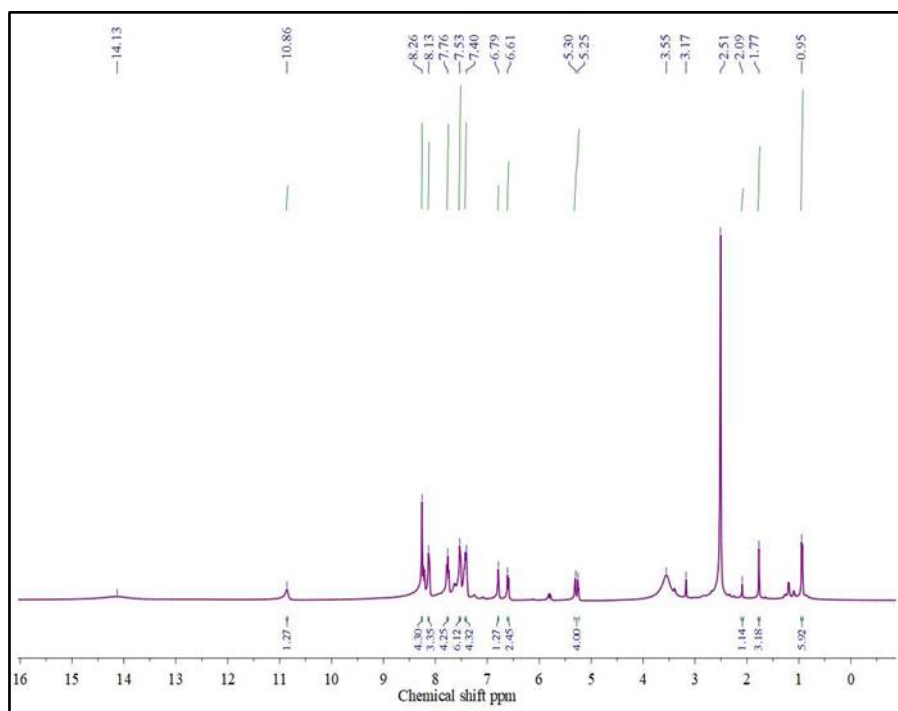


**Figure 4.9:**  $^1\text{H}$  NMR spectrum of complex C2

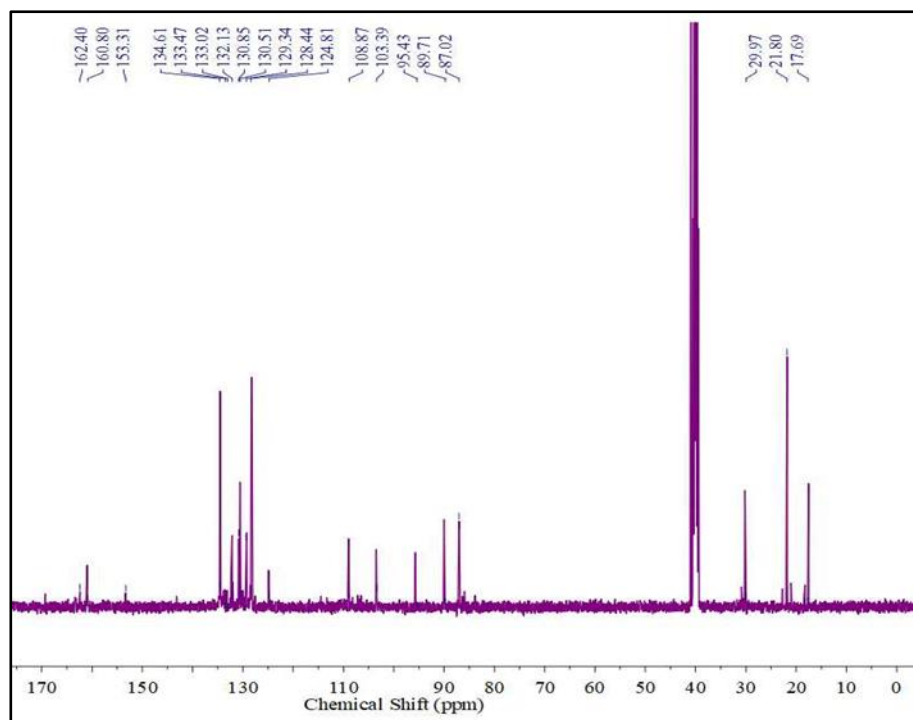


**Figure 4.10:**  $^{13}\text{C}$  NMR spectrum of complex *C2*

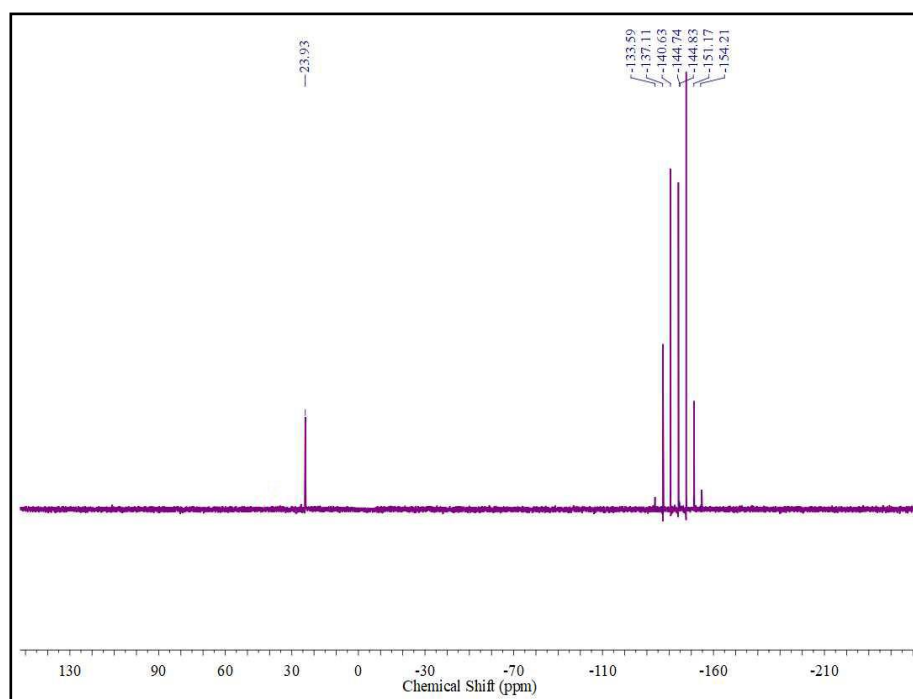


**Figure 4.11:**  $^{31}\text{P}$  NMR spectrum of complex *C2*

#### 4.3.2.4 NMR Spectra of Complex *C3*

$^1\text{H}$  NMR (500.13 MHz, 298 K, DMSO- $d_6$ )  $\delta$ , ppm: 13.63, 9.90 [s, 1H, H of N-H and O-H], 8.27-6.32 [ligand aromatic protons], 6.21-6.05

[*p*-cymene aromatic proton], 2.90 [m, 1H, CH(CH<sub>3</sub>)<sub>2</sub>], 2.00 [s, 3H, CH of C<sub>6</sub>H<sub>4</sub>CH<sub>3</sub>], 1.19 [d, 6H, CH of C(CH<sub>3</sub>)<sub>2</sub>], 4.45-4.00 [PTA protons]<sup>26</sup>. <sup>13</sup>C NMR (125 MHz, DMSO-d<sub>6</sub>) δ, ppm: 154.4 [C of NH-C=N], 162.4, 161.1 [C of C-OH], 124.5, 126.8, 128.4, 129.3, 130.7, 108.5, 107.6, 105.5, 103.5 [C of ligand], 88.6, 85.5 [C of *p*-cymene], 88.8, 85.7 [C of NCH<sub>2</sub>N], 71.9, 71.5 [C of NCH<sub>2</sub>P], 30.6 [CH of *p*-cymene], 22.2 [C(CH<sub>3</sub>)<sub>2</sub> of *p*-cymene], 21.7 [CH<sub>3</sub> of *p*-cymene]. <sup>31</sup>P NMR (126 MHz, DMSO-d<sub>6</sub>) δ, ppm: -29.53 [s, PTA], -144.19 [sept, PF<sub>6</sub>] [27].

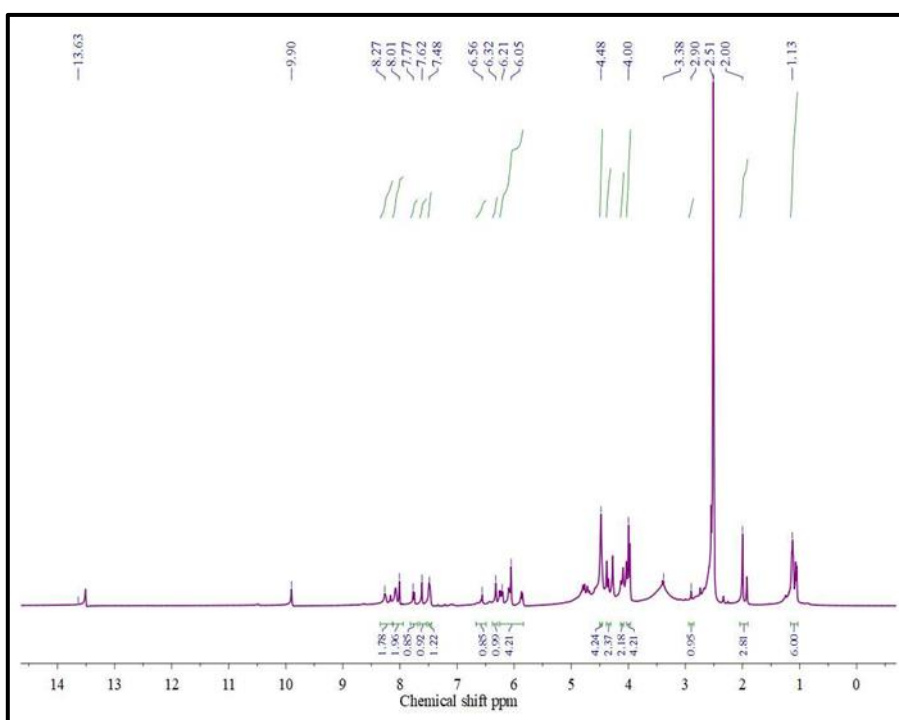


**Figure 4.12:** <sup>1</sup>H NMR spectrum of complex C3

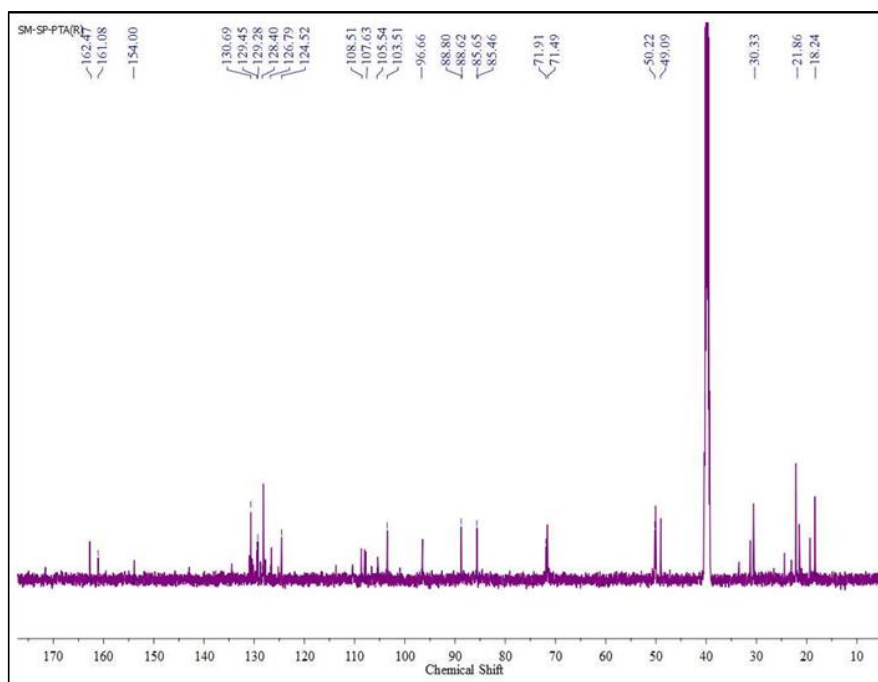


**Figure 4.13:**  $^{13}\text{C}$  NMR spectrum of complex C3

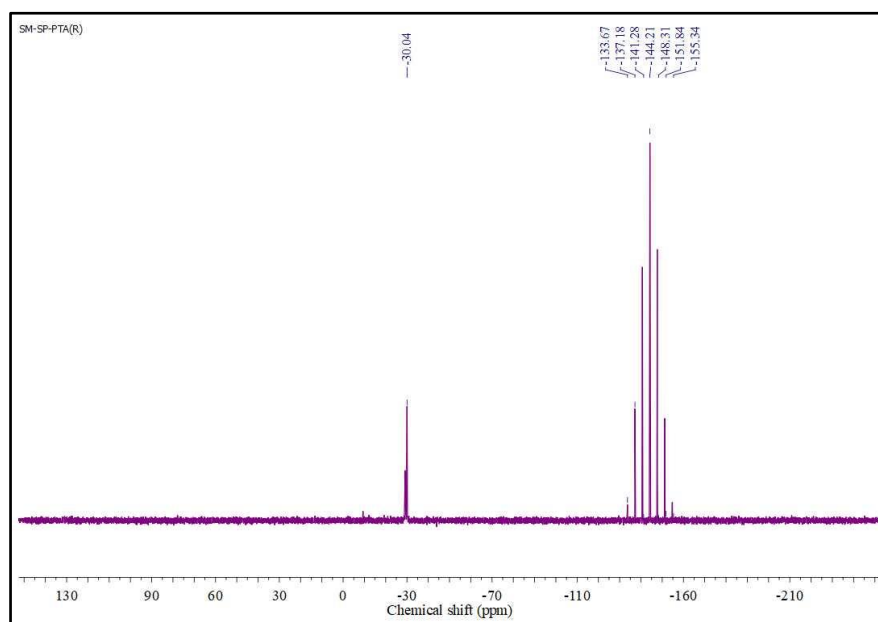


**Figure 4.14:**  $^{31}\text{P}$  NMR spectrum of complex C3

### 4.3.3 FTIR Spectra

The bands in the IR-spectra matched well with the expected characteristic bands of various functional groups of the ligand, complexes and the nanoparticles. The FTIR spectra of complexes C1,

**C2**, **C3** and ligand (Figure 4.15) exhibited a band at around  $1600\text{ cm}^{-1}$  corresponding to C=N functionality [28]. The band for N-H and O-H stretching frequency were found to be overlapping in the region of  $3200\text{-}3460\text{ cm}^{-1}$ . The band at  $1230\text{-}1240\text{ cm}^{-1}$  corresponds to aromatic C-O stretching frequency. The presence of characteristic bands at  $526$  and  $540\text{ cm}^{-1}$  in the IR spectrum of **C2** and **C3** corresponds to Ru-P stretching frequency signifying successful complexation with ruthenium [29]. Bands at  $831$  and  $821\text{ cm}^{-1}$  in case of complex **C2** and **C3** arises due to P-F stretching frequency of the counter anion [30].

As evident from the IR spectra (Figure 4.16) of **MSNs**, **A-MSNs** as well as **C2@A-MSNs**, bands at  $1072$ ,  $794$  and  $456\text{ cm}^{-1}$  correspond to the Si-O bonds of silanol groups. In case of pristine **MSNs** bands at  $3364\text{ cm}^{-1}$  corresponding to deformation of vibration of interlayer water and  $1642\text{ cm}^{-1}$  corresponding to OH stretching vibration of silanol groups confirmed the presence of bare silanol groups on the surface [31]. The band at  $1560\text{ cm}^{-1}$  corresponding to bending vibration mode of N-H confirmed the successful functionalization of the **MSNs** with amine groups [21]. The presence of imine band at  $1604\text{ cm}^{-1}$  confirmed the successful loading of ruthenium complex on **A-MSNs**. Also, the shift of OH band from  $3300\text{ cm}^{-1}$  (free complex B) to  $3029\text{ cm}^{-1}$  (**C2@A-MSNs**) indicates H-bonding interaction between the polar groups present in the complex and the amine groups of **A-MSNs** [20].

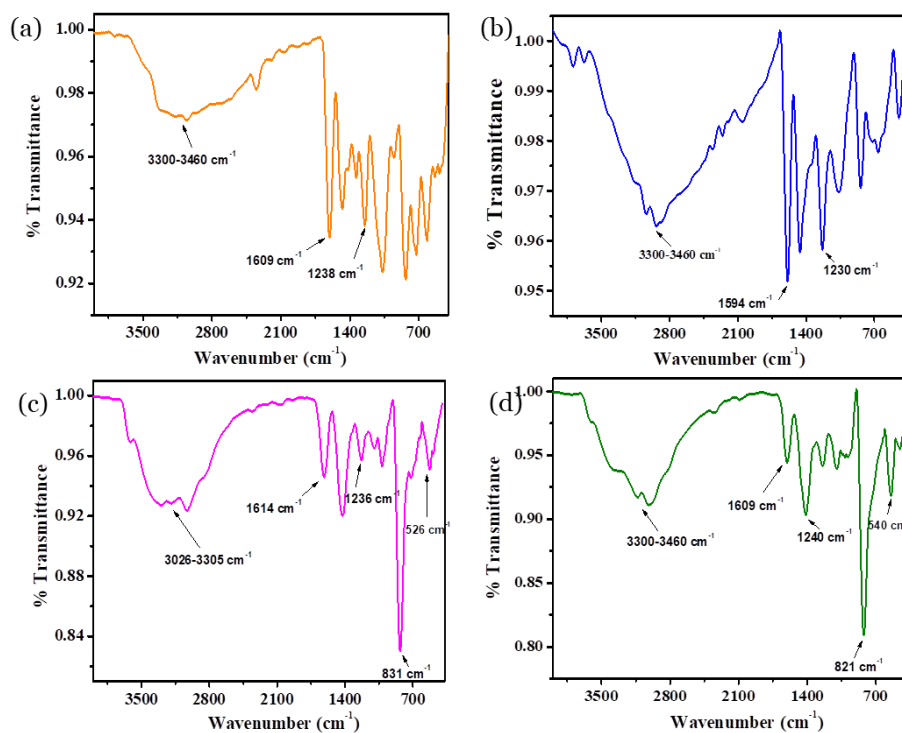


**Figure 4.15:** FTIR Spectra of (a) Ligand **HL** (b) complex **C1**, (c) complex **C2**, (d) complex **C3**

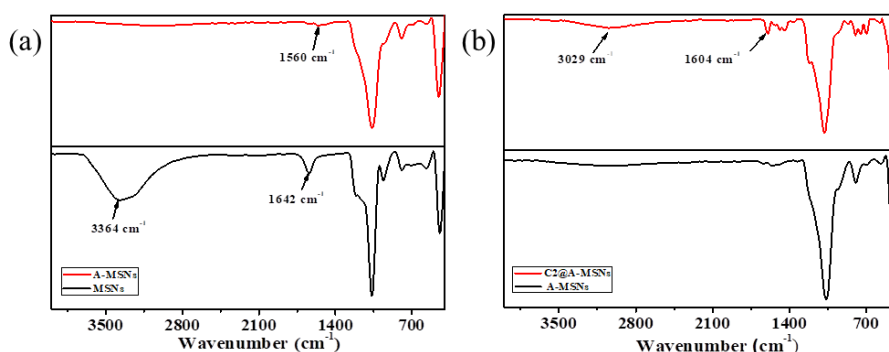


**Figure 4.16:** FTIR Spectra depicting (a) amine functionalization of MSNs (b) Loading of **C2** on A-MSNs

#### 4.3.4 UV-Vis Spectra

The UV-Vis spectra (Figure 4.17a) of ligand (**HL**) and the complexes show two peaks, one in the region of 275-280 nm which corresponds to  $\pi \rightarrow \pi^*$  transition and another peak of lower intensity in the 340-360 nm region which corresponds to  $n \rightarrow \pi^*$  transitions. An additional peak

in the range of 390-400 nm is observed only in the case of metal complexes which correspond to MLCT transition [32].

The successful loading of the ruthenium complex on amine functionalized MSNs was further confirmed from the presence of the absorption bands corresponding to **C2** (Figure 4.17b). The blue shift observed for  $n \rightarrow \pi^*$  transition occurs due to H-bonding between amine groups of **A-MSNs** and polar groups of complex [33].

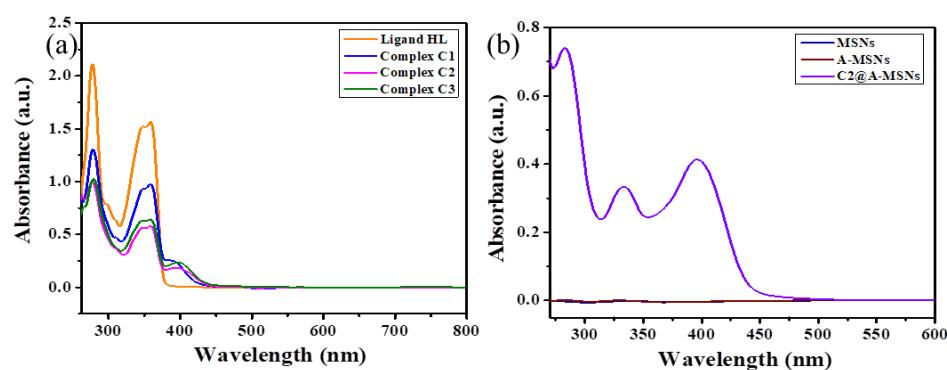


**Figure 4.17:** UV- Vis absorption spectra of (a) ligand **HL** and complexes **C1**, **C2**, **C3** (b) **MSNs**, **A-MSNs** and **C2@A-MSNs**

### 4.3.5 Fluorescence Spectra

As the ligand and the complexes synthesized are fluorescent in nature, their emission spectra were recorded in DMSO by exciting at a wavelength of 360 nm. From the emission spectra (Figure 4.18), it is observed that at 404 nm, ligand **HL** shows the highest fluorescence intensity, followed by complex **C1**, complex **C2** and complex **C3** in decreasing order. Higher intensity bands are observed at 481 nm, with the ligand **HL** showing highest intensity, followed by complex **C1**, complex **C2** and complex **C3**. The excitation and the corresponding emission wavelengths for the three complexes and the ligand are given in Table 4.1.

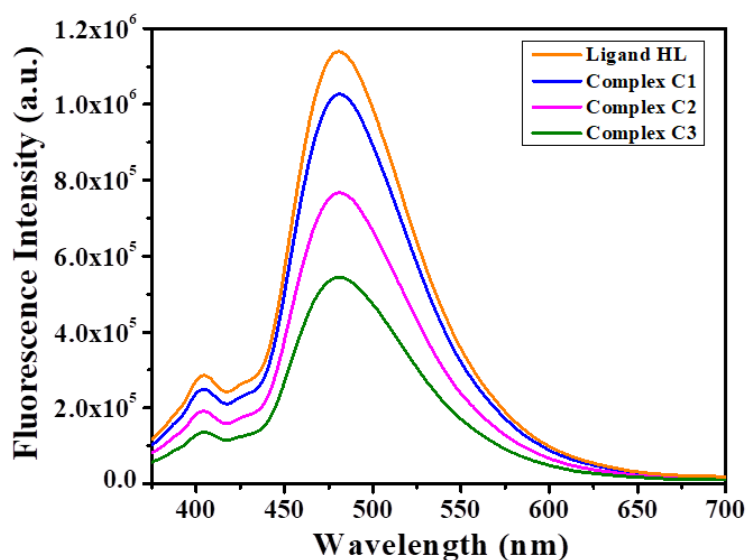


**Figure 4.18:** Fluorescence spectra of ligand **HL** and complexes **C1**, **C2**, **C3**

**Table 4.1:** Excitation and emission wavelengths of ligand **HL** and complexes

	UV-Vis (nm)	$\lambda_{\text{excitation}}$ (nm)	$\lambda_{\text{emission}}$ (nm)
<b>Ligand HL</b>	360, 347	360	404, 480
<b>Complex C1</b>	389, 360, 348	360	403, 481
<b>Complex C2</b>	394, 360, 348	360	403, 481
<b>Complex C3</b>	397, 360, 347	360	404, 480

### 4.3.6 Powder X-ray Diffraction

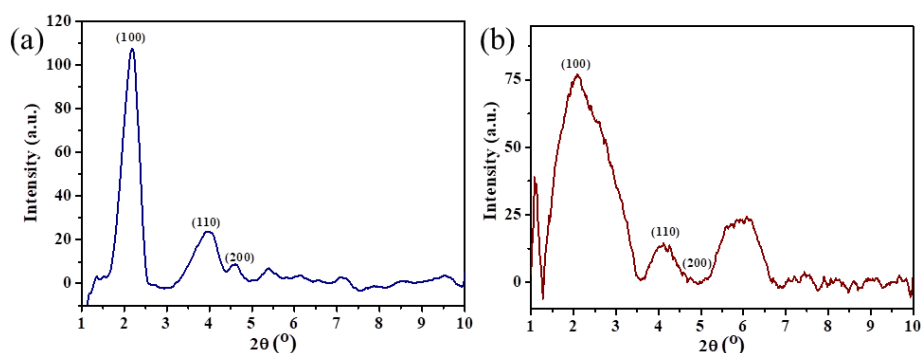


**Figure 4.19:** Powder XRD patterns for (a) **MSN** (b) **A-MSNs**

Before loading the ruthenium complex the nanocarriers was characterized using powder X-ray diffraction. The peaks observed in

the powder X-ray diffraction (Figure 4.19) corresponds to reflections from the 100, 110 and 200 planes confirming the hexagonal mesoporous pattern in MSN and A-MSNs [20]. The broad nature of the peaks also justifies the amorphous nature of the silica nanoparticles.

### 4.3.7 TGA Analysis and N<sub>2</sub> Adsorption-Desorption Isotherm

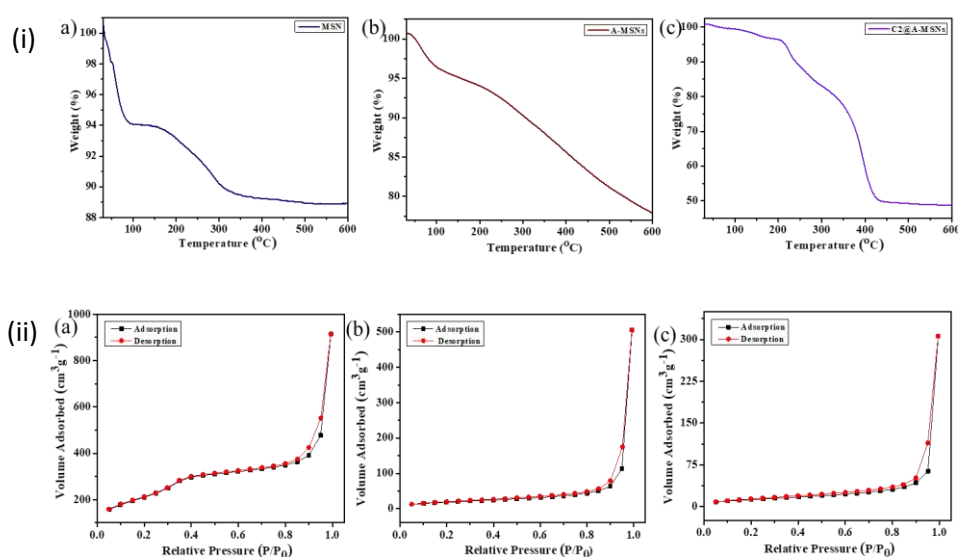


**Figure 4.20** (i) TGA curve of (a) MSNs, (b) A-MSNs, (c) C2@A-MSNs (ii) N<sub>2</sub> adsorption isotherms of (a) MSNs, (b) A-MSNs, (c) C2@A-MSNs

The thermal stability of the synthesized MSNs, A-MSNs and C2@A-MSNs were studied using thermogravimetric analysis (Figure 4.20 (i)). The weight loss up to 100 °C was due to loss of H<sub>2</sub>O molecules. The drug loaded nanoparticles were found to be thermally stable up to 200 °C with no significant weight loss except removal of surface adsorbed water molecules [25].

The mesoporous nature of the nanoparticles was characterized using N<sub>2</sub> adsorption-desorption isotherms (Figure 4.20 (ii)). The decrease in surface area from 752.617 m<sup>2</sup> g<sup>-1</sup> to 68.326 m<sup>2</sup> g<sup>-1</sup> and pore diameter from 1.49202 nm to 1.32461 nm indicates successful functionalization with APTES. The surface area further decreased to 47.093 m<sup>2</sup> g<sup>-1</sup> due to loading of complex C2 on A-MSNs. The loading of drug on A-

MSNs were further justified from the decrease in pore volume from  $2.807 \times 10^{-1} \text{ cc g}^{-1}$  (in MSNs) to  $1.951 \times 10^{-2} \text{ cc g}^{-1}$  (in A-MSNs) to  $1.923 \times 10^{-2} \text{ cc g}^{-1}$  (C2@ A-MSNs) [21]. The various parameters obtained from N<sub>2</sub> adsorption-desorption isotherms are listed in Table 4.2.

**Table 4.2:** Characteristic parameters of MSN and A-MSNs observed from N<sub>2</sub> adsorption-desorption experiment

	BET Surface Area (m <sup>2</sup> g <sup>-1</sup> )	Langmuir Surface Area (m <sup>2</sup> g <sup>-1</sup> )	Pore Volume (cc g <sup>-1</sup> )
MSNs	752.617	2461.722	$2.807 \times 10^{-1}$
A-MSNs	68.326	803.424	$1.951 \times 10^{-2}$
C2@A-MSNs	47.093	786.744	$1.923 \times 10^{-2}$

#### 4.3.8 FE-SEM Analysis

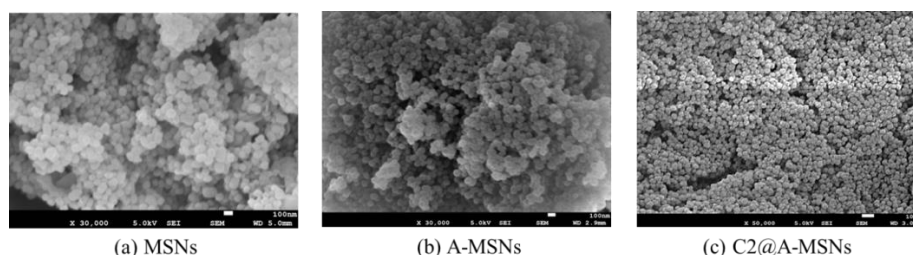


**Figure 4.21:** SEM images of (a) MSNs (b) A-MSNs (c) C2@A-MSNs

The amorphous nature of MSNs, A-MSNs is clearly visible from the SEM images (Figure 4.21). After loading of the ruthenium complex the arrangement and amorphous nature remains intact. However due to the presence of the metal complex the surface seems to be rough.

#### 4.4 Stability Study

For the synthesized complexes to function as potent anticancer drug, it is necessary that they must be stable in biological medium. To check whether the synthesized complexes are stable or not, UV-Vis spectra were recorded at different time intervals. As evident from Figure 4.22 no significant change in peak position was observed indicating that the complexes are sufficiently stable and do not degrade in biological

medium up to twenty-four hours. Since the tumor environment is acidic in nature, pH stability of the complex in acidic environment forms an integral part of the study. The UV-Vis spectra of complex **C2** in PBS buffer solution at pH 5.4 mimicking the tumour environment was recorded at different time intervals. No shift in absorption band indicates that the complex can retain its integrity even at lower pH up to seventy two hours.

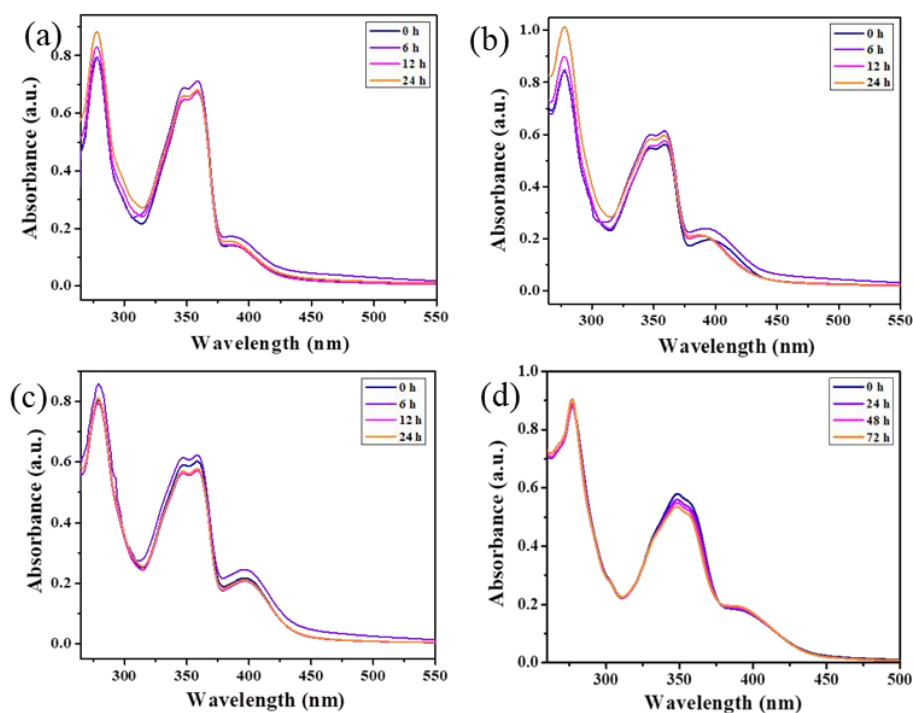


**Figure 4.22:** Stability study of (a) complex **C1**, (b) complex **C2**, (c) complex **C3** in DMSO/PBS buffer solution (d) complex **C2** in PBS buffer (pH- 5.4)

## **4.5 Lipophilicity Study**

The synthesized complexes must cross the lipid bilayer to enter the cancer cells. This property is referred as lipophilicity. To study the lipophilic character of the synthesized complexes, the well-known partition coefficient method was employed where the complexes were dissolved in n-octanol and DMSO: H<sub>2</sub>O mixture and the partition coefficient was calculated. Complex **C2** with triphenylphosphine group has the maximum partition coefficient indicating that it will have the highest cellular uptake among all the three complexes. It is probably

due to the presence of the hydrophobic phenyl rings which can facilitate the transportation of the drug molecule through the lipid bilayer of the cell membrane [26]. Table 4.3 lists the partition coefficient values for the three complexes.

**Table 4.3:** Partition coefficient value for the complexes **C1**, **C2** and **C3**

LIPOPHILICITY STUDY	P <sub>O/W</sub>	log P <sub>O/W</sub>
Complex C1	2.82	0.45
Complex C2	5.87	0.76
Complex C3	1.89	0.27

## **4.6 Protein Binding Study**

### ***4.6.1 Emission Spectra***

The binding of ruthenium complexes with plasma protein needs to be studied in order to check the bioavailability of the drugs. In the blood plasma serum albumin protein (HSA-Human serum albumin or BSA-Bovine serum albumin) is most abundant and plays an essential role in transporting drug molecules to the desired target. Because of Enhanced Permeability and Retention (EPR) effect, the serum proteins are important macromolecular carriers involved in transporting the drugs selectively to the cancer cells [34]. Thus, study of the interaction between the serum proteins and ruthenium complexes forms an integral component in drug designing. The intrinsic fluorescent nature of these proteins due to the presence of amino acids like tryptophan, tyrosine and phenylalanine was used to study their binding property. BSA/HSA exhibits fluorescence mainly due to tryptophan residue. The difference between BSA and HSA is that the former has two residues of tryptophan (Trp-134) and (Trp-212) whereas the latter contains only one (Trp-214) [35]. The tryptophan environment is highly sensitive and any structural change in its vicinity can cause alteration in its fluorescence intensity. Thus, to study how the complexes interact with

HSA/BSA, tryptophan fluorescence quenching experiments was performed.

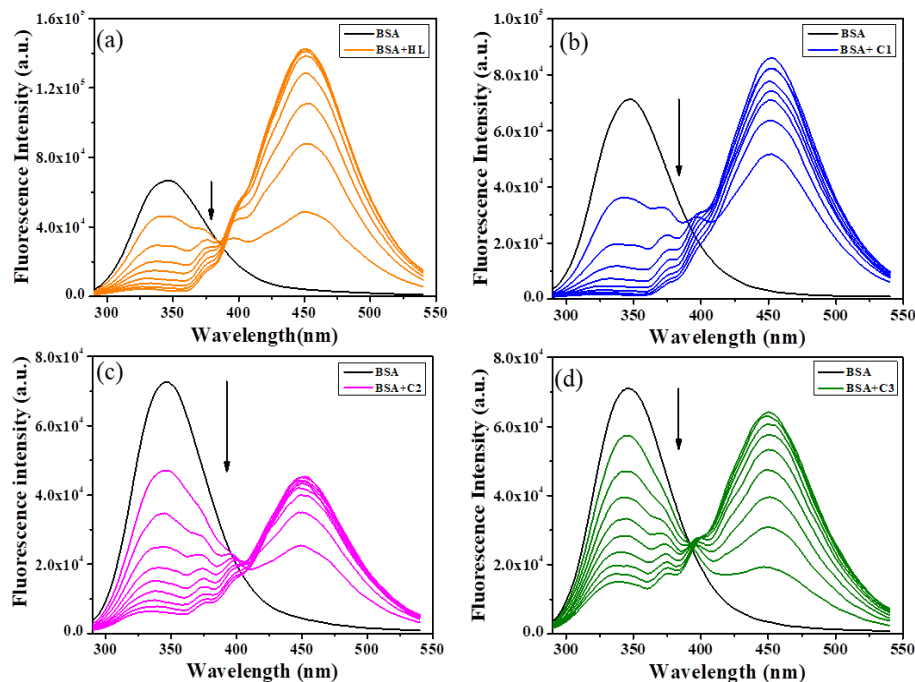


**Figure 4.23:** Fluorometric titration spectra of BSA ( $10 \mu\text{M}$ ) with (a) ligand HL, (b) complex C1, (c) complex C2, and (d) complex C3 at 298 K

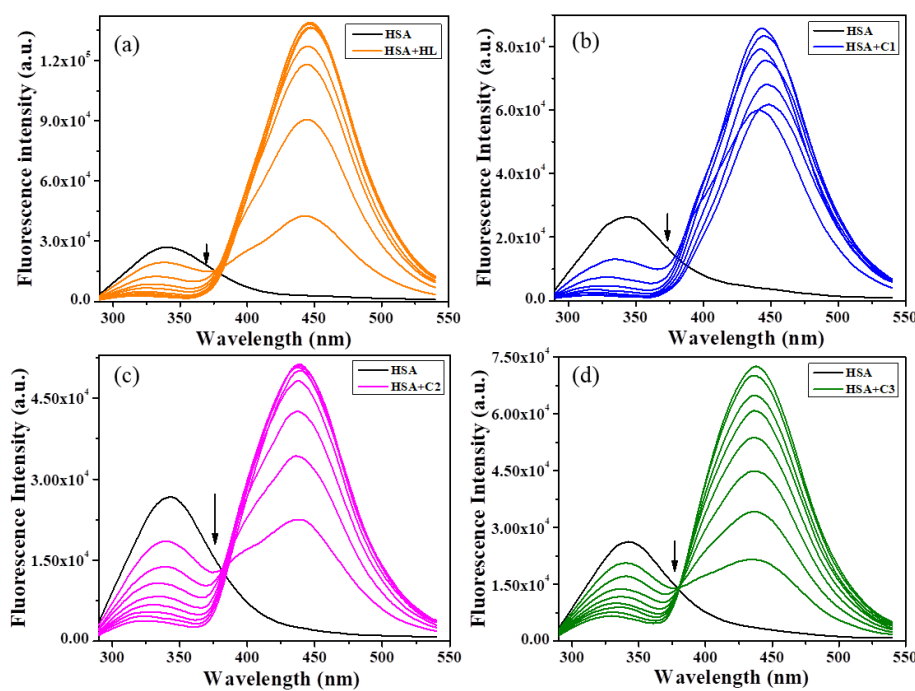


**Figure 4.24:** Fluorometric titration spectra of HSA ( $10 \mu\text{M}$ ) with (a) ligand HL, (b) complex C1, (c) complex C2, and (d) complex C3 at 298 K

It was observed that with increasing concentration of the metal complexes (0-80  $\mu\text{L}$ ), the peak for BSA/HSA at around 335 nm exhibited successive lowering of intensity and at around 445 nm, gradual appearance of a new peak was observed when excitation was carried out at 280 nm (Figure 4.23 and Figure 4.24). The decrease in fluorescence intensity at 335 nm was attributed to the quenching of the original emission of BSA/HSA due to binding of the protein with the complex while the increase in fluorescence intensity at a longer wavelength was observed because of the inherent fluorescence nature of the complexes and the ligand respectively.

To find the binding capacity of the ligand **HL** and the complexes with BSA/ HSA, Stern-Volmer Equation and Scatchard Equations were used and various binding parameters were calculated which are listed in Table 4.4. The  $K_q$  value suggests that the quenching is static quenching [17].

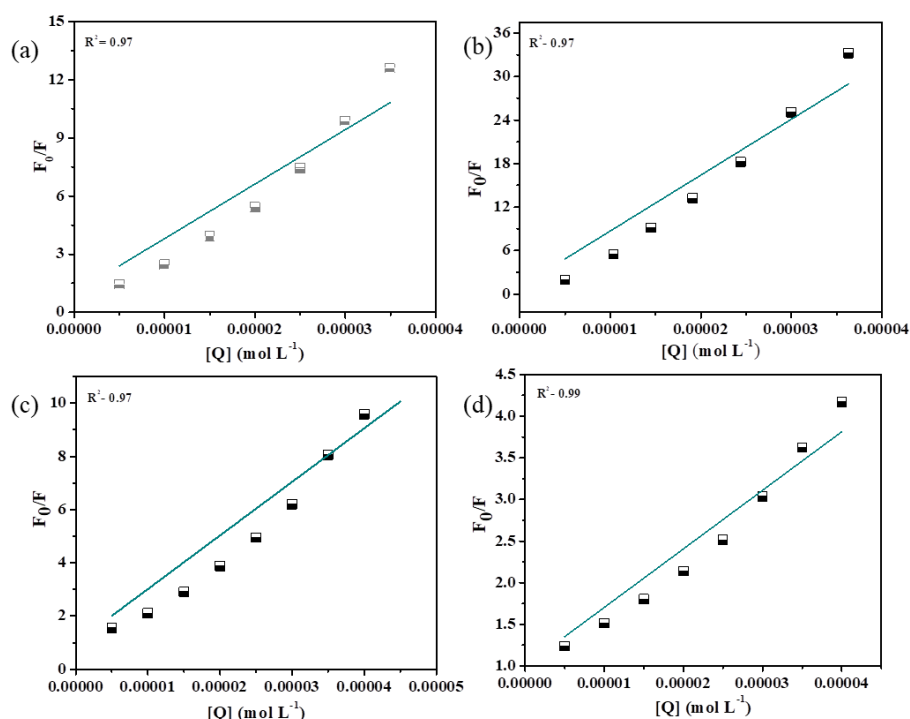


**Figure 4.25:** Stern Volmer plots for the titration of BSA with (a) ligand **HL**, (b) complex **C1**, (c) complex **C2**, (d) complex **C3**

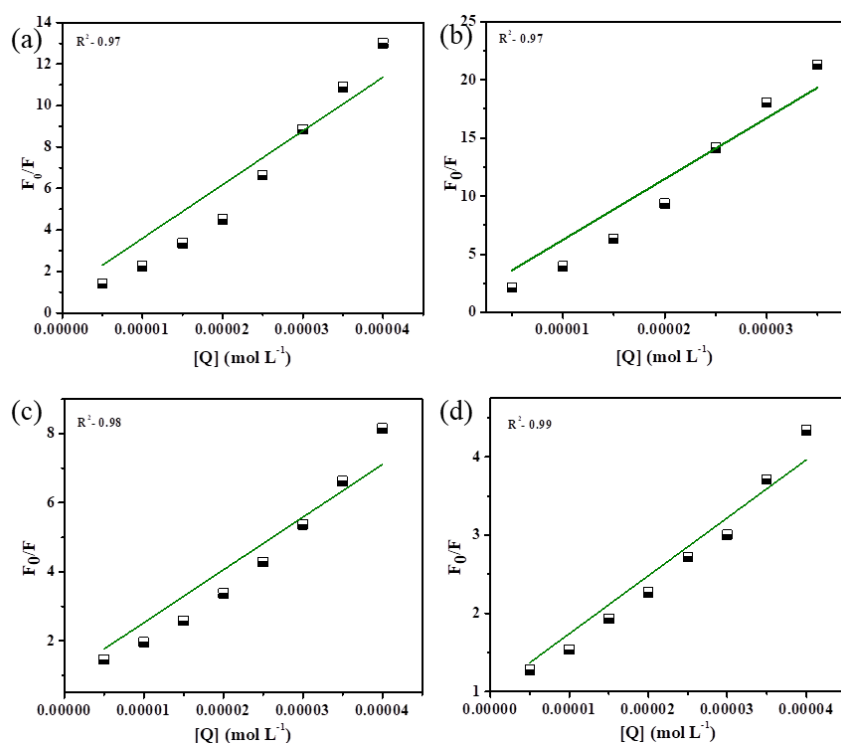


**Figure 4.26:** Stern Volmer plots for the titration of HSA with (a) ligand HL, (b) complex C1, (c) complex C2, (d) complex C3

**Table 4.4:** Various parameters to analyze the binding between proteins and the compounds from SV and Scatchard plots.

Compound	$K_{sv}(M^{-1})$	$K_q(M^{-1}s^{-1})$	$K_a(M^{-1})$	n
<b>BSA</b>				
Ligand (HL)	$2.8 \times 10^5$	$4.5 \times 10^{13}$	$3.5 \times 10^8$	1.68
Complex C1	$8.9 \times 10^5$	$1.4 \times 10^{14}$	$8.7 \times 10^9$	1.89
Complex C2	$2.0 \times 10^5$	$3.2 \times 10^{13}$	$9.1 \times 10^6$	1.37
Complex C3	$7.4 \times 10^4$	$1.2 \times 10^{13}$	$1.0 \times 10^6$	1.26
<b>HSA</b>				
Ligand (HL)	$2.5 \times 10^5$	$4 \times 10^{13}$	$2.0 \times 10^8$	1.64
Complex C1	$5.2 \times 10^5$	$8.4 \times 10^{13}$	$1.2 \times 10^9$	1.52
Complex C2	$1.5 \times 10^5$	$2.4 \times 10^{13}$	$4.0 \times 10^6$	1.32
Complex C3	$7.4 \times 10^4$	$1.2 \times 10^{13}$	$5.5 \times 10^5$	1.19

## 4.7 Nucleic Acid Binding Study

Binding of ruthenium complexes to nucleic acids can cause conformational changes which can ultimately lead to inhibition of cell division [36]. Thus, investigating the interaction of the synthesized complexes with DNA and probing their mode of binding is essential.

### 4.7.1 Absorption Spectra

To investigate the mode of binding of the ruthenium complexes with DNA, UV-Vis absorption spectrum was recorded. Complexes can bind to DNA through groove binding or intercalation. Intercalation is depicted by a decrease in absorbance whereas groove binding is depicted by an increase in absorbance. When a fixed amount of ruthenium complex or ligand was titrated with increasing amount of CT-DNA, hypochromism or decrease in absorbance was observed which suggests intercalation mode of binding with DNA (Figure 4.27). The planar aromatic rings of the ligand intercalate between the DNA base pairs through  $\pi$ - $\pi$  stacking [36].

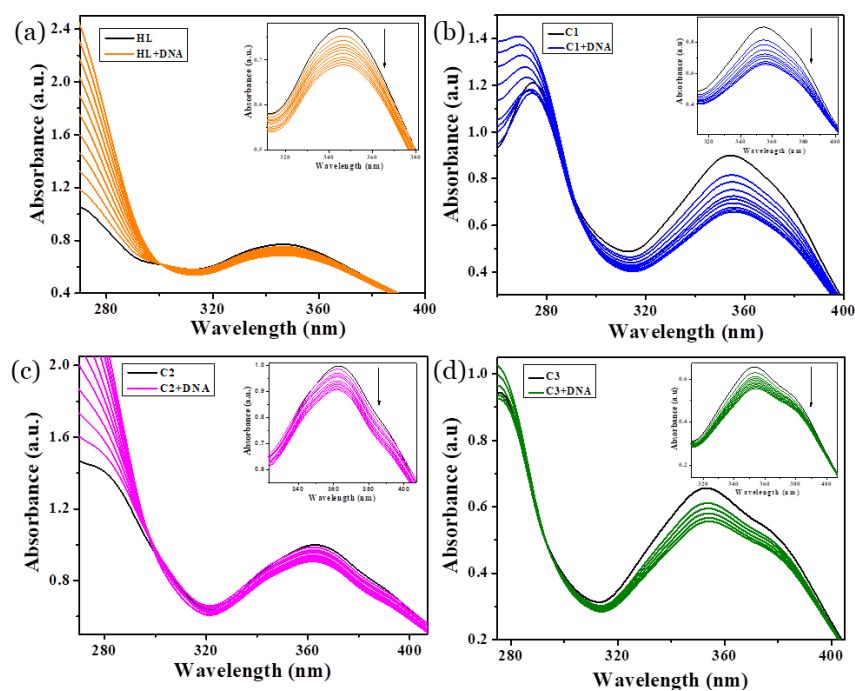


**Figure 4.27:** Titration of (a) ligand **HL**, (b) complex **C1**, (c) complex **C2**, and (d) complex **C3** with increasing amount of CT- DNA at 298 K using UV-Vis spectroscopy

### 4.7.2 Emission Spectra

To further confirm the intercalation mode of binding, ethidium bromide (EtBr) an intercalating dye was used to study competitive fluorometric displacement assay. Ethidium bromide intercalates between the base pairs of DNA causing it to show fluorescent property. When to a fixed concentration of DNA-EtBr solution, increasing amount of the synthesized complexes and ligand was added, decrease in fluorescence intensity was observed (Figure 4.28) indicating intercalation of the complexes between base pairs. The ruthenium complex competes with ethidium bromide and displaces it causing a decrease in fluorescence intensity. Thus, the results of emission spectra are in accordance with absorption spectra. The competitive fluorometric displacement assay using EtBr was also performed with RNA which exhibited similar results suggesting intercalative mode of binding (4.29). Thus, intercalation of the ruthenium complexes alters the base pair spacing thereby leading to helix unwinding [36]. Using the fluorometric data, Stern Volmer equation and Scatchard Equation the quenching parameters were calculated which are listed in Table 4.5.

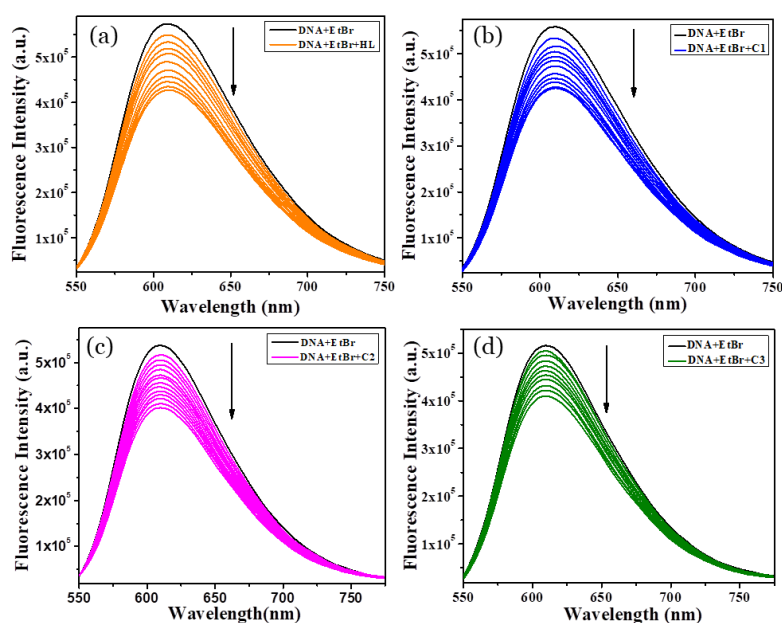


**Figure 4.28:** Fluorometric titration spectra of CT-DNA ( $10 \mu\text{M}$ ) with (a) ligand HL, (b) complex C1, (c) complex C2, and (d) complex C3 at 298 K

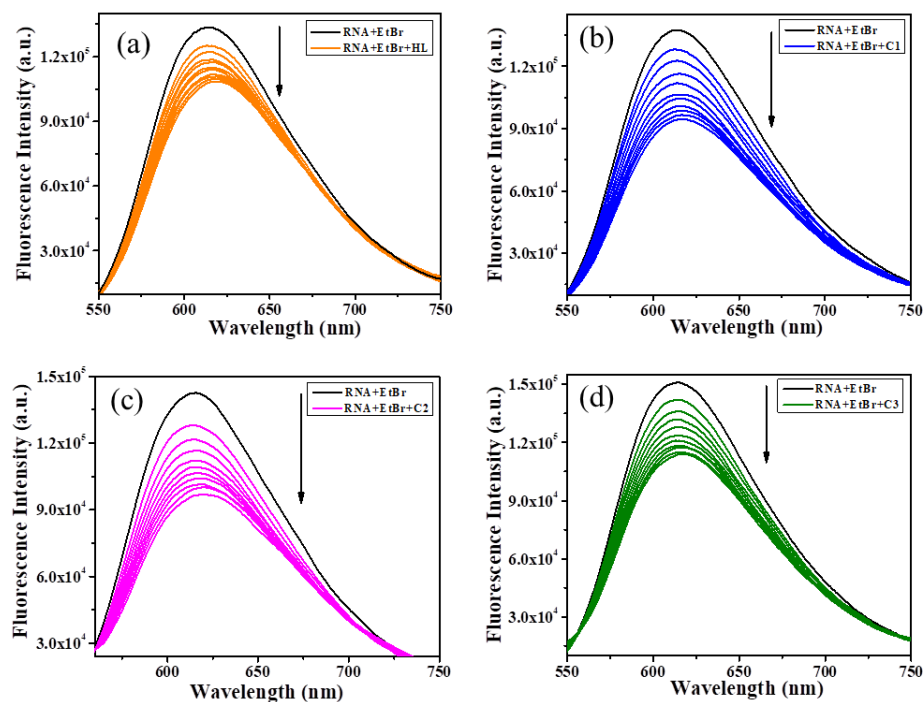


**Figure 4.29:** Fluorometric titration spectra of RNA ( $10 \mu\text{M}$ ) with (a) ligand HL, (b) complex C1, (c) complex C2, and (d) complex C3 at 298 K

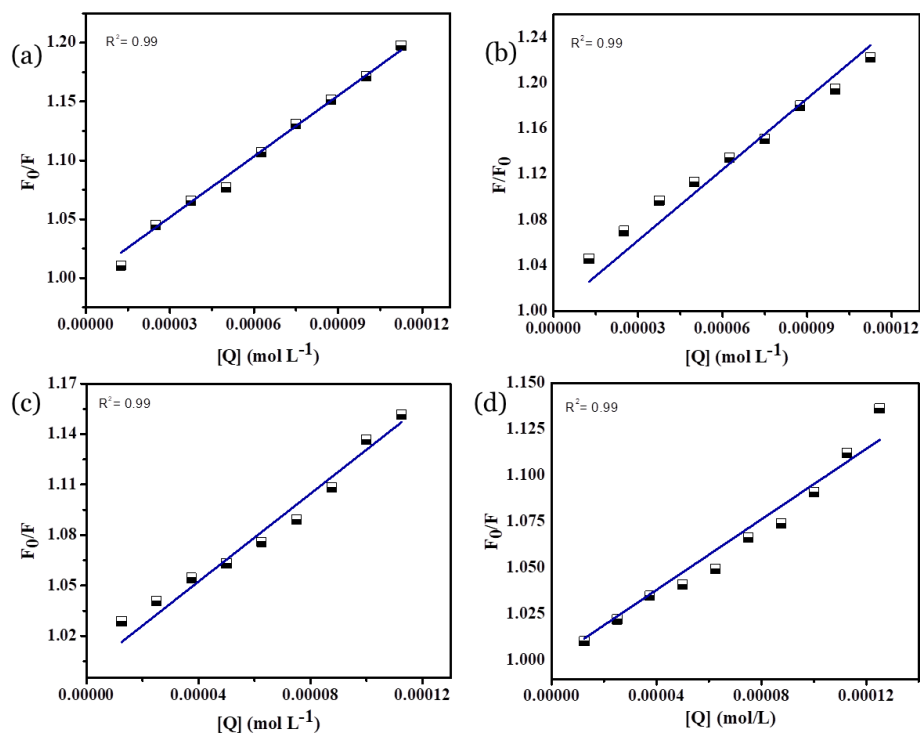


**Figure 4.30:** Stern Volmer plots for binding of DNA with (a) ligand HL, (b) complex C1, (c) complex C2, (d) complex C3

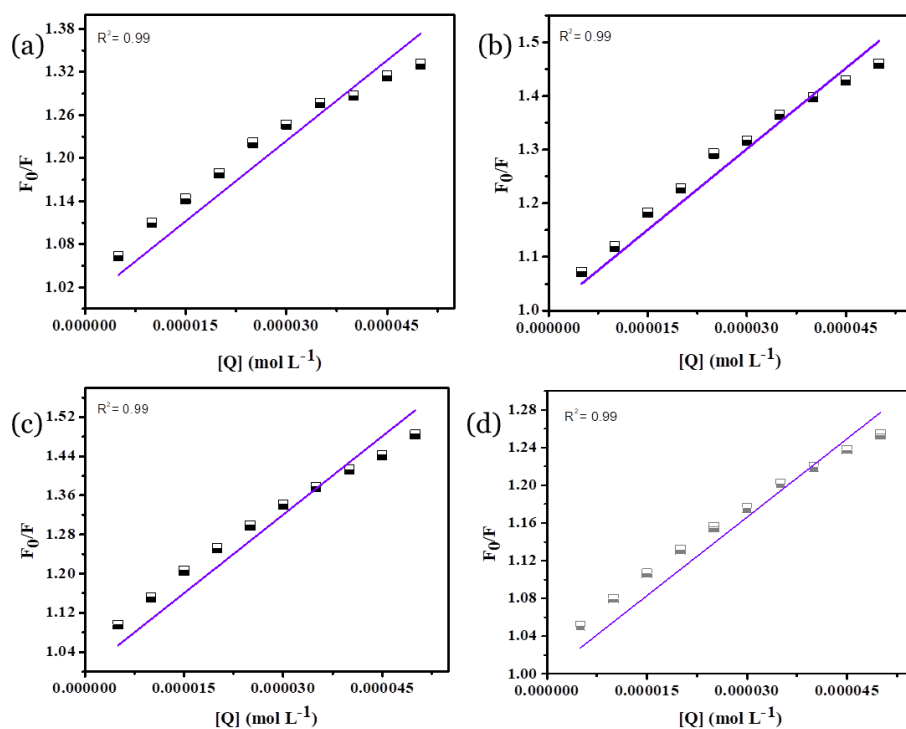


**Figure 4.31:** Stern Volmer plots for binding of DNA with (a) ligand HL, (b) complex C1, (c) complex C2, (d) complex C3

**Table 4.5:** Various parameters to analyze the binding between nucleic acids and the compounds from SV and Scatchard plot

Compound	$K_{sv}(M^{-1})$	$K_q(M^{-1}s^{-1})$	$K_a(M^{-1})$	n
<b>DNA</b>				
<b>Ligand (HL)</b>	$1.2 \times 10^3$	$4.5 \times 10^{12}$	$2.4 \times 10^3$	1.02
<b>Complex C1</b>	$1.9 \times 10^4$	$2.4 \times 10^{13}$	$7.3 \times 10^4$	1.45
<b>Complex C2</b>	$1.4 \times 10^4$	$3.2 \times 10^{13}$	$5.1 \times 10^4$	1.37
<b>Complex C3</b>	$1.6 \times 10^3$	$1.2 \times 10^{13}$	$3.8 \times 10^3$	1.10
<b>RNA</b>				
<b>Ligand (HL)</b>	$7.4 \times 10^3$	$4 \times 10^{13}$	$4.53 \times 10^3$	1.24
<b>Complex C1</b>	$1.0 \times 10^4$	$8.4 \times 10^{13}$	$1.6 \times 10^4$	1.82
<b>Complex C2</b>	$1.0 \times 10^4$	$2.4 \times 10^{13}$	$2.36 \times 10^4$	1.62
<b>Complex C3</b>	$5.5 \times 10^3$	$1.2 \times 10^{13}$	$3.6 \times 10^3$	1.30

## 4.8 Drug Loading and pH Stimulated Release

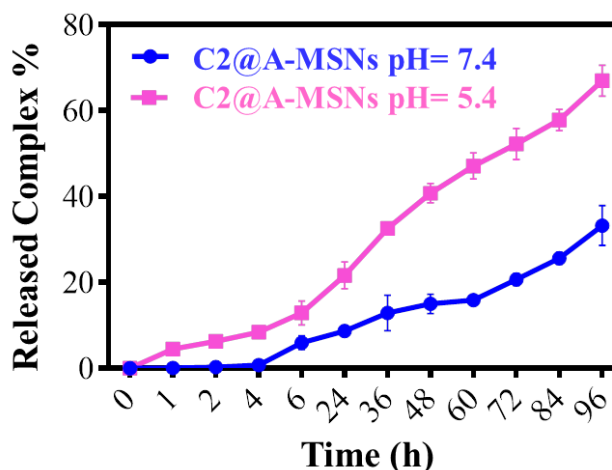


*Figure 4.32: Drug release profile for C2@A-MSNs in acidic and neutral pH*

Efficient drug loading is necessary for proper release and function of these nanocarriers. It was found that nanosystem **C2@A-MSNs** has a drug loading capacity about 40.4% (40.4 mg/100 mg). Since the cellular environment of cancer cells has a lower pH than normal cells, to mimic the biological environment and check the specificity of the nanocarriers the drug release experiment was performed at two different pH. As observed from the release profile (Figure 4.32), at neutral pH no detectable amount of complex is released up to four hours and after ninety-six hours only around 30% of the drug is released. However, in acidic medium drug release is observed even at initial stage (though small amount) and after ninety-six hours a significant amount around 65% of the complex is released. The greater release of drug at lower pH may occur due to protonation of the amine groups of **A-MSNs** and hydroxyl group of the metal complex which causes breaking of the hydrogen bonding interactions responsible for holding the drug causing its release in acidic environment (Figure 4.33) [21,25]. To check whether the drug released from **A-MSNs** is same as the one loaded, mass spectrometry was performed and the peak characteristic of the free complex **C2** was obtained at  $m/z=773$  indicating that the integrity of the complex remains intact (Figure 4.34).



**Figure 4.33:** Probable mechanism of drug release from A-MSNs

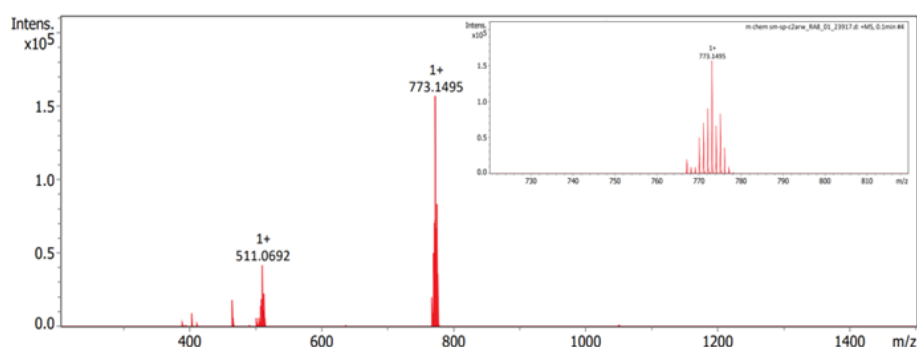


**Figure 4.34:** Mass spectrum of released complex from A-MSNs; ESI-MS ( $m/z$ )  $C_{42}H_{40}N_2O_2PRu$ : Calculated for  $[C_{45}H_{40}N_2O_2PRu]^+$ : 773.19; Found: 773.1495

## **4.9. Cell Viability Assay**

The successful binding of the ruthenium complexes with biomolecules motivated us to further investigate their cytotoxic activity. To check the cytotoxic activity of the synthesized complexes, cell viability was checked using colorimetric MTT assay. The  $IC_{50}$  values were calculated from the cell viability curves (Figure 4.35). All the complexes exhibited significant anticancer activity on HeLa and DU145 cancer cell lines with complex **C2** showing the highest activity with minimum  $IC_{50}$  value (17.78  $\mu$ M for HeLa and 27.42  $\mu$ M for DU145 cells). A probable reason for this enhanced cytotoxicity could be the presence of the hydrophobic phenyl rings which enhances the interaction with biomolecules [26]. It can also be attributed to the highest lipophilic behaviour of complex **C2** which results in greater

accumulation inside the cells. It is noteworthy to mention that all the complexes are active against cisplatin resistant DU145 cells. The cytotoxicity was further enhanced with a significant decrease in  $IC_{50}$  value upon loading the complex **C2** on **A-MSNs**. This was probably due to better cellular internalisation occurring due to interaction between negatively charged phospholipids and positively charged surface of **A-MSNs** [21]. Also, the  $IC_{50}$  value for the free ligand is significantly high indicating the necessity for complexation with ruthenium. The complexes were also treated on HEK 293 normal cell lines and their comparatively higher  $IC_{50}$  value proves their selectivity and target specificity towards cancerous cell only. The  $IC_{50}$  values for the complexes and ligand are represented by histogram (Figure 4.36) and listed in Table 4.6.

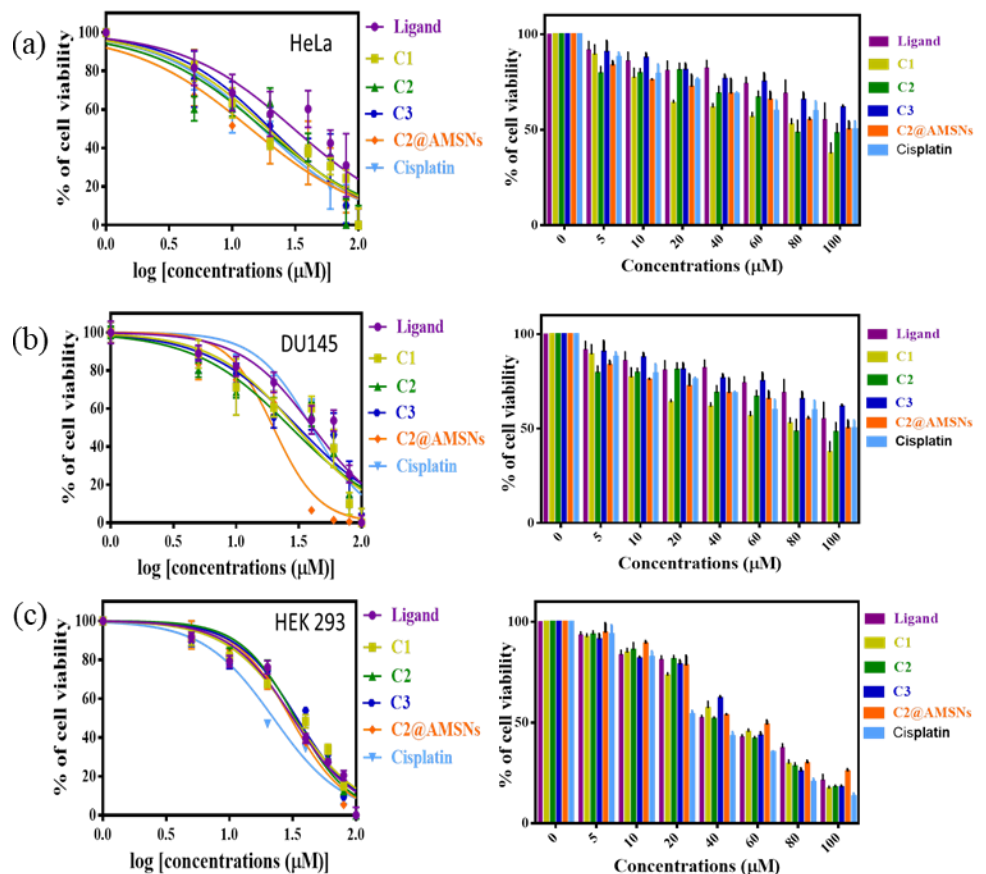


**Figure 4.35:** Cell viability curves for ligand **HL**, complex **C1**, **C2**, **C3** and **C2@A-MSNs** on (a) **HeLa** cell lines (b) **DU145** cell lines and (c) **HEK 293** (normal cell lines)

**Table 4.6:**  $IC_{50}$  values in ( $\mu M$ ) of the ligand, three complexes and C2@A-MSNs for cancer cells lines HeLa and DU145 and normal cells HEK 293

	HeLa	DU145	HEK 293
<b>Ligand HL</b>	$30.79 \pm 0.56$	$41.13 \pm 0.53$	$32.28 \pm 0.45$
<b>Complex C1</b>	$19.21 \pm 0.43$	$30.11 \pm 0.83$	$33.73 \pm 0.51$
<b>Complex C2</b>	$17.78 \pm 0.48$	$27.42 \pm 0.58$	$34.59 \pm 0.59$
<b>Complex C3</b>	$20.26 \pm 0.36$	$31.46 \pm 0.74$	$36.21 \pm 0.44$
<b>C2@A-MSNs</b>	$14.01 \pm 0.43$	$19.83 \pm 0.75$	$31.83 \pm 0.39$
<b>Cisplatin</b>	$17.40 \pm 0.38$	$40.22 \pm 0.59$	$23.18 \pm 0.28$

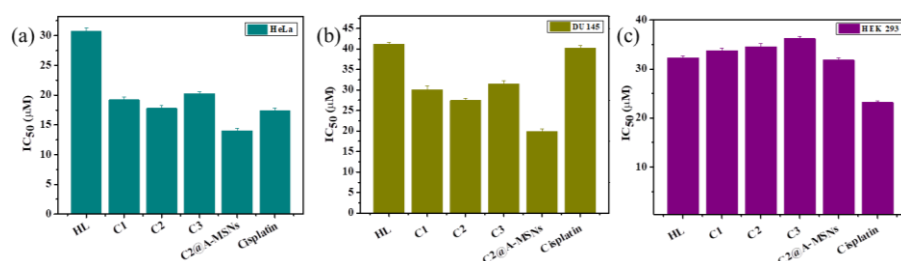


**Figure 4.36:** Histogram representing the  $IC_{50}$  values in ( $\mu M$ ) of the ligand, three complexes and C2@A-MSNs for cancer cells lines (a) HeLa, (b) DU145 and (c) normal cells HEK 293

#### **4.10 Apoptosis Study using Dual Staining Method**

To investigate whether the complexes can cause apoptosis of cancer cells and study the morphological changes occurring accompanied during apoptosis, the dual staining assay was performed using acridine orange (AO) and ethidium bromide (EtBr). AO is a membrane permeable dye capable of staining cells having membranes intact. It emits green fluorescence upon binding to DNA. EtBr is a membrane impermeable dye and can thus cause staining of cells with ruptured membrane and shows bright red fluorescence on binding to DNA or apoptotic bodies [37]. The confocal microscopy images (Figure 4.37) show that all the synthesized complexes can cause apoptosis in cancer cells with complex C2 and C2@A-MSNs showing significantly better results. Certain morphological changes like rupturing of cell membrane

and fragmented nuclei are observed which are characteristic of apoptosis [17].

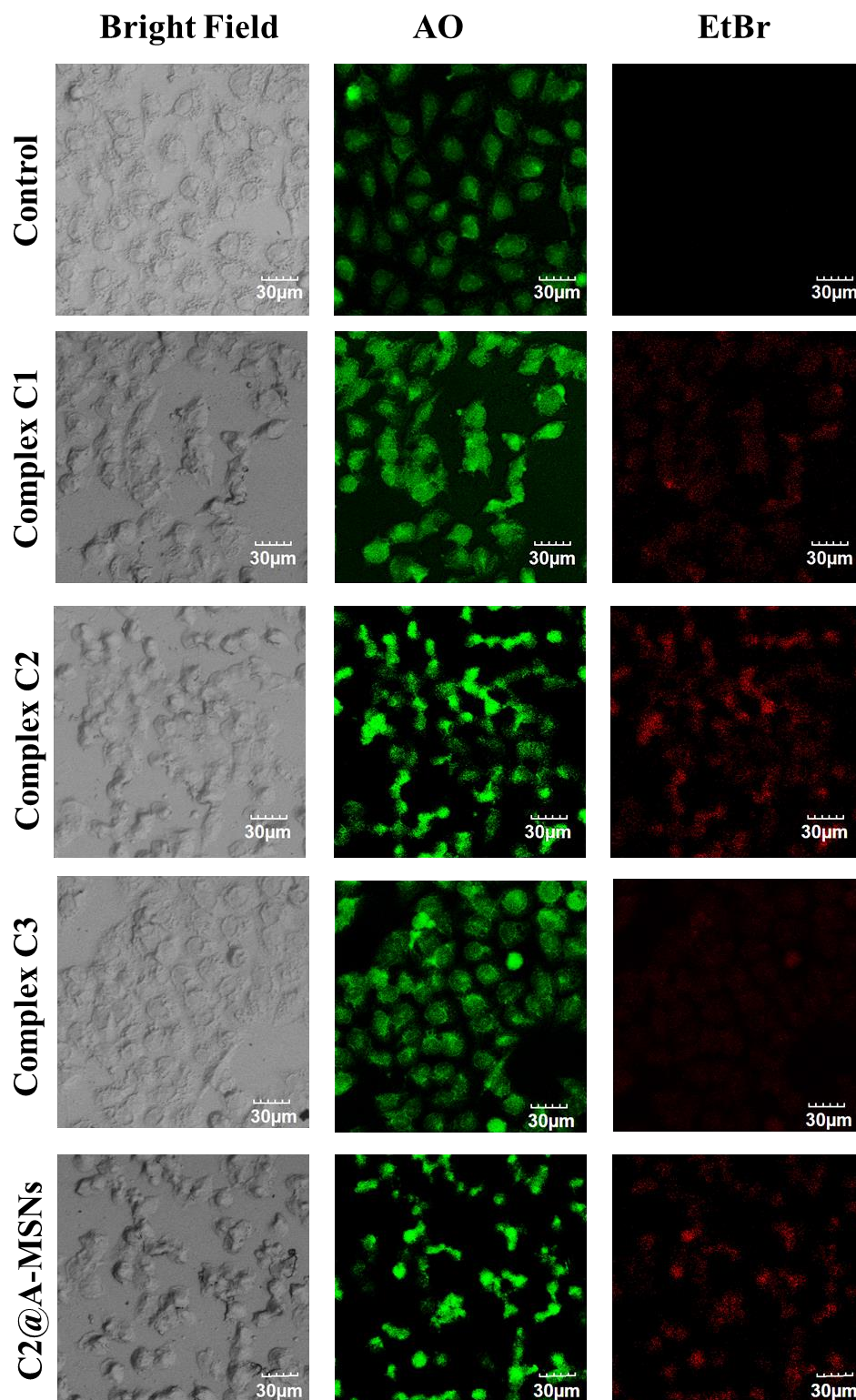


*Figure 4.37: Confocal images of HeLa cells stained with AO and EtBr after treatment with the complexes*

## 4.11 ROS Generation- DCFH-DA Staining

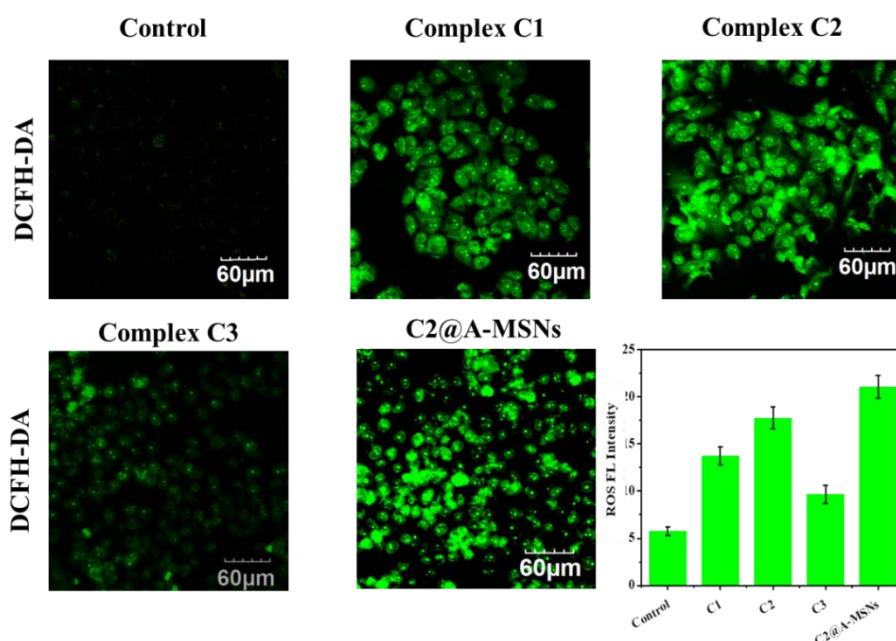


**Figure 4.38:** ROS generation using DCFH-DA Assay and fluorescence intensity graph for ROS generation

Generation of reactive oxygen species is an efficient way of inducing cell death by producing oxidative stress inside the cells and causing damage to intracellular substances. Generation of ROS in quantities greater than what can be scavenged by the cellular enzymes like superoxide dismutase (SOD) causes oxidative damage to the cells. Also, cancer cells because of their rapid multiplying nature require a greater amount of oxygen as compared to normal cells. Thus, converting oxygen into reactive oxygen species like superoxide anion, hydrogen peroxide and  $\text{OH}^\bullet$  can hamper the cell division process thereby causing cell death [38]. Thus, the synthesized complexes were investigated for their ability to generate ROS using the DCFH-DA staining method. DCFH-DA (Dichloro-dihydro-fluorescein diacetate) is a dye which in the presence of ROS gets oxidized to DCF which emits green fluorescence [39]. Thus, it can be used for the detection of ROS. The microscope images Figure (4.38) clearly show green fluorescence only in the case of treated cells and not in the control suggesting that the ruthenium complexes are capable of generating ROS which are responsible for the green fluorescence.

## 4.12 Metastasis Inhibition

Metastasis refers to the spread of cancer cells from malignant parts of the body to non-malignant cells and tissues. Controlling the spread of tumor cells to normal cells at an early stage is thus necessary to treat cancer [17]. To investigate the antimetastatic property of the synthesized complexes wound healing assay was performed where cancer cells were treated with  $IC_{50}$  concentration value of the complexes and the wound coverage area was monitored after twenty-four hours. All the complexes exhibited antimetastatic property (Figure 4.39) and could inhibit the migration of cancer cells when compared to control (no treatment given). However, complex **C2** inhibited cell migration to the maximum extent with a wound closure ratio of 35%. The antimetastatic property was further enhanced upon treating the cells with **C2@A-MSNs**.

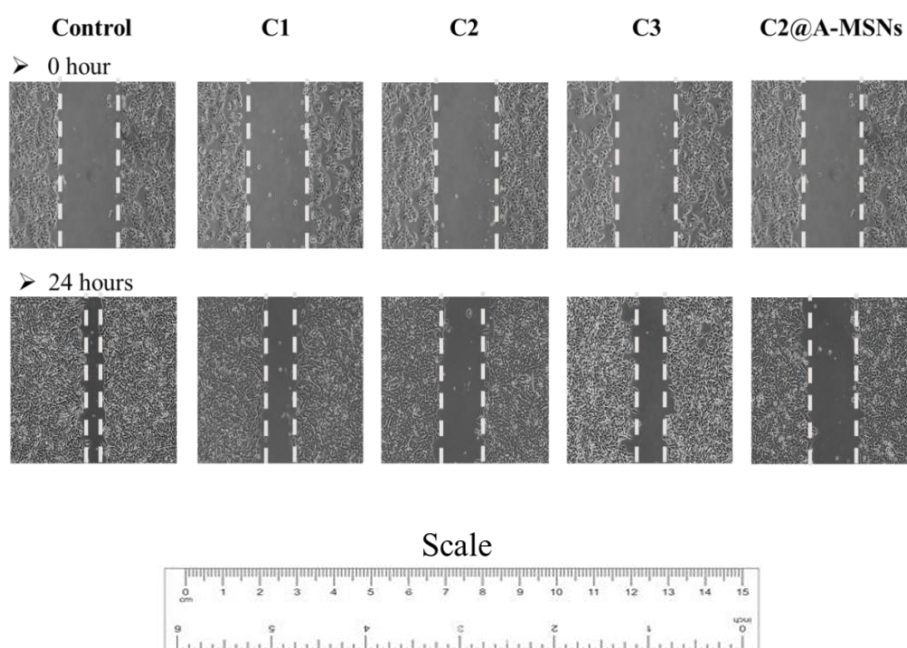


**Figure 4.39:** Wound healing motility assay of HeLa untreated and treated cell with the free complexes as well as **C2@A-MSNs**. Images were taken at 0 and 24 h

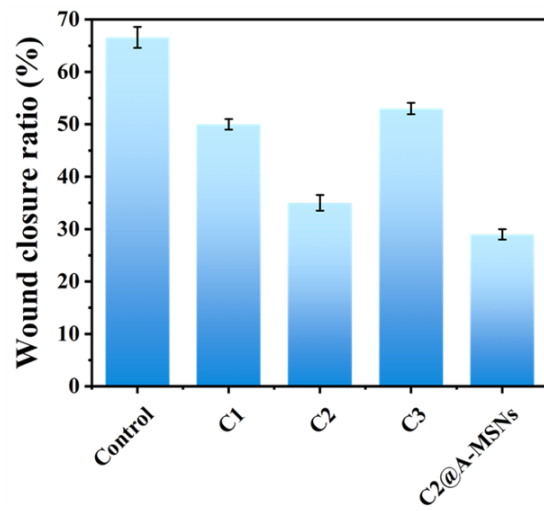


*Figure 4.40: Histogram representing percentage wound closure ratio after 24 hours*

## Chapter 5

### CONCLUSION AND FUTURE SCOPE

Three ruthenium(II) arene complexes with *p*-cymene as the arene group and having a bidentate benzimidazole based chelating ligand with N and O as donor sites have been synthesized. The co-ligands have been varied between chloride, PPh<sub>3</sub> (triphenylphosphine) and PTA (1,3,5-triaza-7-phosphaadamantane). The complexes were characterized using several spectroscopic techniques like ESI-MS, IR, NMR and UV-Vis spectroscopy and their molecular formula are found to be [Ru(η<sup>6</sup>-*p*-cym)(L)Cl], [Ru(η<sup>6</sup>-*p*-cym)(L)PPh<sub>3</sub>]PF<sub>6</sub>, [Ru(η<sup>6</sup>-*p*-cym)(L)PTA]PF<sub>6</sub>. Both the ligand and the complexes are found to be fluorescent in nature. The complexes were studied for their lipophilic behaviour and complex **C2** was found to be most lipophilic. All the complexes are stable in biological medium upto twenty four hours. Tryptophan quenching experiments suggested that the complexes significantly bind to albumin proteins like BSA and HSA. As evident from absorption and emission spectroscopy the complexes are also potent of binding to CT-DNA and RNA and the mode of binding was found to be intercalation. Cytotoxicity study was performed on HeLa and DU145 cells and all the complexes showed anticancer activity with better results on HeLa cells. Among all the three complexes, complex **C2** exhibited the lowest IC<sub>50</sub> value and highest anticancer activity due to the presence of the hydrophobic triphenylphosphine group which lead to its better cellular internalization as demonstrated by lipophilicity study. The hydrophobic phenyl rings also had better interaction with the biomolecules as compared to chloride or PTA. Since complex **C2** was the most potent anticancer drug among the three complexes, it was loaded on amine functionalized mesoporous silica nanoparticles to see whether these drug delivery nanocarriers can enhance their therapeutic performance. As observed from the cytotoxicity study, the anticancer activity was improved upon loading and their selectivity for cancer cells also increased. The complexes

were also studied for their apoptotic properties, ROS generating ability and anti-metastatic behaviour on HeLa cell lines and complex **C2** and **C2@A-MSNs** were found to exhibit better results. In conclusion, the above synthesized complexes can act as potent anticancer agents and the study can be further taken to *in vivo* tumour models.

## **REFERENCES**

- [1] Thun M. J., DeLancey J. O., Center M. M., Jemal A., Ward E. M. (2010) The Global Burden of Cancer: Priorities for Prevention, *Carcinogenesis*, 31 (1), 100–110. (DOI:10.1093/carcin/bgp263)
- [2] Franz K. J., Metzler-Nolte N. (2019), Introduction: Metals in Medicine, *Chem. Rev.*, 119 (2), 727–729. (DOI:10.1021/acs.chemrev.8b00685)
- [3] Zeng L., Gupta P., Chen Y., Wang E., Ji L., Chao H., Chen Z. S. (2017) The Development of Anticancer Ruthenium(II) Complexes: From Single Molecule Compounds to Nanomaterials, *Chem. Soc. Rev.*, 46 (19), 5771–5804. (DOI:10.1039/C7CS00195A)
- [4] Pragti, Kundu B. K., Mukhopadhyay S. (2021), Target Based Chemotherapeutic Advancement of Ruthenium Complexes, *Coord. Chem. Rev.*, 448, 214169-214209. (DOI:10.1016/j.ccr.2021.214169)
- [5] Cepeda V., Fuertes M. A., Castilla J., Alonso C., Quevedo C., Pérez J. M. (2007) Biochemical Mechanisms of Cisplatin Cytotoxicity, *Anticancer Agents Med. Chem.*, 7 (1), 3–18. (DOI:10.2174/187152007779314044)
- [6] van Rijt S. H., Sadler P. J. (2009), Current Applications and Future Potential for Bioinorganic Chemistry in the Development of Anticancer Drugs, *Drug Discov. Today*, 14 (23), 1089–1097. (DOI:10.1016/j.drudis.2009.09.003)
- [7] Kenny R. G., Marmion C. J. (2019), Toward Multi-targeted Platinum and Ruthenium Drugs—A New Paradigm in Cancer Drug Treatment Regimens?, *Chem. Rev.*, 119(2), 1058-1137. (DOI:10.1021/acs.chemrev.8b00271)
- [8] Ferraro M. G., Piccolo M., Misso G., Santamaria R., Irace C. (2022), Bioactivity and Development of Small Non-Platinum Metal-Based Chemotherapeutics, *Pharmaceutics*, 14 (5), 954-987. (DOI:10.3390/pharmaceutics14050954)

- [9] Reedijk J. (2012), Fast and Slow versus Strong and Weak Metal–DNA Binding: Consequences for Anti-Cancer Activity. *Metallomics*, 4 (7), 628–632. (DOI:10.1039/c2mt20032e)
- [10] Alessio E. (2017), Thirty Years of the Drug Candidate NAMI-A and the Myths in the Field of Ruthenium Anticancer Compounds: A Personal Perspective, *Eur. J. Inorg. Chem.*, 12, 1549-1560.(DOI:10.1002/ejic.201600986)
- [11] Hartinger C. G., Zorbas-Seifried S., Jakupec M. A., Kynast B., Zorbas H., Keppler B. K. (2006), From Bench to Bedside-Preclinical and Early Clinical Development of the Anticancer Agent Indazolium Trans-[Tetrachlorobis(1H-Indazole)Ruthenate(III)] (KP1019 or FFC14A). *J. Inorg. Biochem.*, 100 (5–6), 891–904. (DOI:10.1016/j.jinorgbio.2006.02.013)
- [12] Alessio E., Messori L. (2019), NAMI-A and KP1019/1339, Two Iconic Ruthenium Anticancer Drug Candidates Face-to-Face: A Case Story in Medicinal Inorganic Chemistry. *Molecules*, 24 (10), 1995-2015. (DOI:10.3390/molecules24101995)
- [13] Dacsi L., Elias H., Frey U., Hoernig A., Koelle U., Merbach A. E., Schneider J. S. (1995), pi.-Arene Aqua Complexes of Cobalt, Rhodium, Iridium, and Ruthenium: Preparation, Structure, and Kinetics of Water Exchange and Water Substitution, *Inorg. Chem.*, 34(1), 306-315. (DOI:10.1021/ic00105a048)
- [14] Hung Y., Kung W. J., Taube H. (1981), Aquo Chemistry of Monoarene Complexes of Osmium(II) and Ruthenium(II), *Inorg. Chem.*, 20 (2), 457–463. (DOI:10.1021/ic50216a028)
- [15] Sonkar C., Sarkar S., Mukhopadhyay S. (2022), Ruthenium(II)–Arene Complexes as Anti-Metastatic Agents, and Related Techniques, *RSC Med. Chem.*, 13 (1), 22–38. (DOI:10.1039/D1MD00220A)
- [16] Sahyon H. A., El-Bindary A. A., Shoair A. F., Abdellatif A. (2018), Synthesis and Characterization of Ruthenium(III) Complex Containing 2-Aminomethyl Benzimidazole, and Its

- Anticancer Activity of in Vitro and in Vivo Models, *J. Mol. Liq.*, 255, 122–134. (DOI:10.1016/j.molliq.2018.01.140)
- [17] Praggi, Kundu B. K., Upadhyay S. N., Sinha N., Ganguly R., Grabchev I., Pakhira S., Mukhopadhyay S. (2022), Pyrene-Based Fluorescent Ru(II)-Arene Complexes for Significant Biological Applications: Catalytic Potential, DNA/Protein Binding, Two Photon Cell Imaging and in Vitro Cytotoxicity, *Dalton Trans.*, 51 (10), 3937–3953. (DOI:10.1039/D1DT04093F)
- [18] Shrivastava N., Naim M. J., Alam M. J., Nawaz F., Ahmed S., Alam O. (2017), Benzimidazole Scaffold as Anticancer Agent: Synthetic Approaches and Structure–Activity Relationship, *Arch. Pharm.*, 350(6), e201700040. (DOI:10.1002/ardp.201700040)
- [19] Martínez-Alonso M., Busto N., Jalón F. A., Manzano B. R., Leal J. M., Rodríguez A. M., García B., Espino G. (2014), Derivation of Structure-Activity Relationships from the Anticancer Properties of Ruthenium(II) Arene Complexes with 2-Aryldiazole Ligands, *Inorg. Chem.*, 53 (20), 11274–11288. (DOI:10.1021/ic501865h)
- [20] Kotcherlakota R., Barui A. K., Prashar S., Fajardo M., Briones D., Rodríguez-Diéguez, A., Patra C. R., Gómez-Ruiz S. (2016), Curcumin Loaded Mesoporous Silica: An Effective Drug Delivery System for Cancer Treatment, *Biomater. Sci.* 2016, 4 (3), 448–459. (DOI:10.1039/C5BM00552C)
- [21] Martínez-Carmona M., Ho Q. P., Morand J., García A., Ortega E., Erthal L. C. S., Ruiz-Hernandez E., Santana M. D., Ruiz J., Vallet-Regí M., Gun'ko Y. K. (2020), Amino-Functionalized Mesoporous Silica Nanoparticle-Encapsulated Octahedral Organoruthenium Complex as an Efficient Platform for Combatting Cancer, *Inorg. Chem.*, 59(14):10275-10284. (DOI:10.1021/acs.inorgchem.0c01436)
- [22] Pettinari R., Marchetti F., Condello F., Pettinari C., Lupidi G., Scopelliti R., Mukhopadhyay S., Riedel T., Dyson P. J. (2014),

- Ruthenium(II)–Arene RAPTA Type Complexes Containing Curcumin and Bisdemethoxycurcumin Display Potent and Selective Anticancer Activity, *Organometallics* 2014, 33 (14), 3709–3715. (DOI:10.1021/om500317b)
- [23] Praggi, Kundu B. K., Sonkar C., Ganguly R., Mukhopadhyay S. (2021), Modulation of Catalytic and Biomolecular Binding Properties of Ruthenium(II)-Arene Complexes with the Variation of Coligands for Selective Toxicity against Cancerous Cells. *Polyhedron*, 207, 115379-115388. (DOI:10.1016/j.poly.2021.115379)
- [24] Tao Z., Toms B., Goodisman J., Asefa T. (2010), Mesoporous Silica Microparticles Enhance the Cytotoxicity of Anticancer Platinum Drugs, *ACS Nano*, 4 (2), 789–794. (DOI:10.1021/nn9015345)
- [25] Kundu B. K., Praggi, Carlton Ranjith W. A., Shankar U., Kannan R. R., Mobin S. M., Bandyopadhyay A., Mukhopadhyay S. (2022), Cancer-Targeted Chitosan-Biotin-Conjugated Mesoporous Silica Nanoparticles as Carriers of Zinc Complexes to Achieve Enhanced Chemotherapy In Vitro and In Vivo, *ACS Appl. Bio Mater.*, 5 (1), (DOI:10.1021/acsabm.1c01041)
- [26] Porwal P., Nayek S., Singh S., Sonawane A., Grabchev I., Ganguly R., Mukhopadhyay S. (2023), Studies on Anticancer Properties with Varying Co-Ligands in Ru(II) Arene Benzimidazole System, *Dalton Trans.*, Advance Article (DOI:10.1039/D3DT00528C)
- [27] Mandal P., Malviya N., Kundu B. K., Dhankhar S. S., Nagaraja C. M.; Mukhopadhyay, S. (2018), RAPTA Complexes Containing N-Substituted Tetrazole Scaffolds: Synthesis, Characterization and Antiproliferative Activity, *Appl. Organomet. Chem.*, 32 (3), e4179. (DOI:10.1002/aoc.4179)
- [28] Beurskens P. T., Cras J. A., Van der Linden J. G. M. (1970), Preparation, Structure, and Properties of Bis(N,N-Di-n-Butyldithiocarbamato)Gold(III) Bromide and Bis(N,N-Di-n-

- Butyldithiocarbamato)Gold(III) Tetrabromoaurate(III), *Inorg. Chem.*, 9 (3), 475–479. (DOI:10.1021/ic50085a009)
- [29] Małecki J. G., Maroń A. (2012), A Ruthenium (II) Hydride Carbonyl Complex with 4-phenylpyrimidine as co-ligand, *Transition Met Chem*, 37, 727-734. (DOI:10.1007/s11243-012-9644-x)
- [30] Adeloye A. O., Olomola T. O., Adebayo A. I., Ajibade P. A. (2012), A High Molar Extinction Coefficient Bisterpyridyl Homoleptic Ru(II) Complex with Trans-2-Methyl-2-Butenoic Acid Functionality: Potential Dye for Dye-Sensitized Solar Cells, *Int. J. Mol. Sci.*, 13 (3), 3511–3526. (DOI:10.3390/ijms13033511)
- [31] Qin P., Yang Y., Li W., Zhang J., Zhou Q., Lu M. (2018), Amino-Functionalized Mesoporous Silica Nanospheres (MSN-NH<sub>2</sub>) as Sorbent for Extraction and Concentration of Synthetic Dyes from Foodstuffs Prior to HPLC Analysis, *Anal. Methods*, 11 (1), 105–112. (DOI:10.1039/C8AY02215A)
- [32] Ramadan R. M., Elsheemy W. M., Hassan N. S., Abdel Aziz A. A. (2018), Synthesis, Spectroscopic Characterization, Thermal Behaviour, in Vitro Antimicrobial and Anticancer Activities of Novel Ruthenium Tricarbonyl Complexes Containing Monodentate V-Shaped Schiff Bases, *Appl. Organomet. Chem.*, 32 (3), e4180. (DOI:10.1002/aoc.4180)
- [33] Brealey G. J., Kasha M. (1955), The Rôle of Hydrogen Bonding in the  $n \rightarrow \pi^*$  Blue-Shift Phenomenon<sup>1</sup>, *J. Am. Chem. Soc.*, 77 (17), 4462–4468. (DOI:10.1021/ja01622a006)
- [34] Ang W. H., Daldini E., Juillerat-Jeanneret L., Dyson P. J. (2007), Strategy to Tether Organometallic Ruthenium-Arene Anticancer Compounds to Recombinant Human Serum Albumin, *Inorg. Chem.*, 46 (22), 9048–9050. (DOI:10.1021/ic701474m)
- [35] Belatik A, Hotchandani S, Carpentier R, Tajmir-Riahi HA (2012) Locating the Binding Sites of Pb(II) Ion with Human and

- Bovine Serum Albumins. PLOS ONE 7(5): e36723. (DOI:10.1371/journal.pone.0036723)
- [36] Devi C. S., Thulasiram B., Satyanarayana S., Nagababu P. (2017), Analytical Techniques Used to Detect DNA Binding Modes of Ruthenium(II) Complexes with Extended Phenanthroline Ring, *J. Fluoresc.*, 27 (6), 2119–2130. (DOI:10.1007/s10895-017-2151-x)
- [37] Liu K., Liu P., Liu R., Wu X. (2015), Dual AO/EB Staining to Detect Apoptosis in Osteosarcoma Cells Compared with Flow Cytometry, *Med. Sci. Monit. Basic Res.*, 21, 15–20. (DOI:10.12659/MSMBR.893327)
- [38] Nakamura H., Takada K. (2021), Reactive Oxygen Species in Cancer: Current Findings and Future Directions, *Cancer Sci.*, 112 (10), 3945–3952. (DOI:10.1111/cas.15068)
- [39] Kim H., Xue X. (2020), Detection of Total Reactive Oxygen Species in Adherent Cells by 2',7'-Dichlorodihydrofluorescein Diacetate Staining, *J. Vis. Exp.*, 160, (DOI:10.3791/60682)